Reduced terrestrial evaporation increases atmospheric water vapor by generating cloud feedbacks

M. M. Laguë[1,2], G. R. Quetin[3], W. R. Boos[4,5]

[1]Coldwater Lab, Center for Hydrology, University of Saskatchewan, Canmore, AB, Canada
[2]Department of Atmospheric Sciences, University of Utah, Salt Lake City, UT, USA
[3]Department of Geography, University of California, Santa Barbara, CA, USA
[4]Department of Earth and Planetary Science, University of California, Berkeley, CA, USA
[5]Climate and Ecosystem Sciences Division, Lawrence Berkeley National Laboratory, Berkeley, CA, USA

Abstract

Reduced terrestrial evaporation directly warms the surface by reducing latent cooling, but also indirectly modifies surface climate by altering atmospheric processes. We use a global climate model to explore two end cases of terrestrial evaporation, comparing the climate of SwampLand, a world where land is always fully saturated with water, to that of DesertLand, where land is always completely lacking in soil moisture. When we suppress evaporation to create a desert-like planet, we find that temperatures increase and precipitation decreases in the global mean. We find an increase in atmospheric water vapor over both land and ocean in the DesertLand simulation. Suppressing evaporative cooling over the continents reduces continental cloud cover, allowing more energy input to the surface and increasing surface moist static energy over land. The residence time of atmospheric water vapor increases by about 50 percent. Atmospheric feedbacks such as changes in air temperatures and cloud cover contribute larger changes to the terrestrial surface energy budget than the direct effect of suppressed evaporation alone. Without the cloud feedback, the land surface still warms with suppressed land evaporation, but total atmospheric water vapor decreases, and the anomalous atmospheric circulations over the continents are much shallower than in simulations with cloud changes; that is, the cloud feedback changes the sign of the water vapor response. This highlights the importance of accounting for atmospheric feedbacks when exploring land surface change impacts on the climate system.

Corresponding author: M. M. Laguë, `marysa.lague@utah.edu`

1 Introduction

Changes in terrestrial evapotranspiration directly impact climate. Reducing evaporation from the land surface has a direct warming effect by reducing energy loss from the land surface (Shukla & Mintz, 1982; Fraedrich et al., 1999; Davin et al., 2010; Laguë et al., 2019). However, in idealized continental configurations with large land masses, reducing terrestrial evaporation can instead drive terrestrial cooling by reducing atmospheric water vapor concentrations and the strength of the water vapor greenhouse effect (Laguë, Pietschnig, et al., 2021). Changes in atmospheric temperatures and water vapor driven by changes in terrestrial evaporation are not only important for terrestrial surface climate, but also for the global atmospheric energy budget, as changes in atmospheric temperatures, moisture content, and cloud cover driven by terrestrial processes alter the global radiative balance of the atmosphere (Swann et al., 2010, 2012; Boos & Korty, 2016; Laguë & Swann, 2016; Laguë, Swann, & Boos, 2021).

Terrestrial processes are an integral part of the global water cycle. Water evaporates from the oceans, is transported by the atmosphere, and falls as precipitation over the land. Water on the land surface is evaporated or transpired to the atmosphere, stored as ground water, or returned to the ocean as runoff. Terrestrial evapotranspiration is determined by a combination of soil moisture, atmospheric demand for water, terrestrial re-distribution of water and the evaporative properties of vegetation and soils (Monteith, 1965; Bonan, 2008; Eltahir & Bras, 1996), while large-scale climate features, topography, and soil properties modulate soil water available for evapotranspiration (see Kottek et al., 2006, and references therein).

Terrestrial evaporation can be limited both by the availability of water to evaporate and by energy (Budyko, 1961; Vargas Zeppetello et al., 2019). Vegetation can directly modulate transpiration by opening and closing stomata (Jones, 1998; Sellers et al., 1996; Pielke et al., 1998); transpiration can change with both water availability and vegetation controls on leaf area (Bonan, 2008), stomatal properties (Ball et al., 1987; Medlyn et al., 2011), and root depth (Lai & Katul, 2000). Evapotranspiration (ET) has changed over the historical period (Hobeichi et al., 2021), with some regions (e.g. tropical Africa) exhibiting a negative trend in ET from 1980-2018, while other regions (e.g. Europe) show a positive trend. Earth system models project more changes in the future (Swann et al., 2016; Berg et al., 2016), though the response is complex and varies across models, with stomatal closure in response to increased atmospheric CO_2 acting to reduce ET and increased leaf area and atmospheric demand for water acting to increase ET. Changes in evapotranspiration are an expected result of land use change (Wang et al., 2021), vegetation responses to increased atmospheric CO_2 (Field et al., 1995; Sellers et al., 1996; Norby et al., 2010; Donohue et al., 2013; Lemordant et al., 2018), and climate change (Swann et al., 2016; Berg et al., 2016; Collins et al., 2013).

How changes in terrestrial evaporation relate to the water cycle both regionally and globally remains an area of active research (Swann et al., 2016; Berg et al., 2016; Koster et al., 2006; Dirmeyer, 2011, 1994, 2006; Byrne & O'Gorman, 2015, 2016; Seneviratne et al., 2010; Laguë, Pietschnig, et al., 2021). Total atmospheric water vapor is projected to increase in simulations of global warming (Sherwood et al., 2010); while relative humidity over the oceans is expected to remain roughly constant, relative humidity over land is expected to decrease (O'Gorman & Muller, 2010a; Byrne & O'Gorman, 2016). Independent of the radiative effects of CO_2, plant responses to increased atmospheric CO_2 are projected to reduce near-surface relative humidity on land (Swann et al., 2016).

In this study, we explore the effect of extreme end-cases of terrestrial evaporation on global climate for the modern continental configuration: land that is always fully saturated (all land looks like a swamp), versus land that is always fully desiccated (all land looks like a desert). We find that fully suppressing terrestrial evaporation leads to increased water vapor concentrations throughout the atmospheric column over most continental and ocean regions. While terrestrial relative humidity decreases with suppressed evaporation, strong cloud feedbacks enhance the energy content and specific humidity of air over land.

2 Methods

We conduct experiments using two climate models to study how changes in land evaporation impact the atmosphere. We use a radiative kernel to decompose the impact of temperature, moisture, cloud, and albedo changes on the atmospheric energy budget.

2.1 Models

We use a modified version of the Community Earth System Model (CESM) (Hurrell et al., 2013), comprised of the Community Atmosphere Model v. 5 (CAM5) coupled to a slab ocean model (Neale et al., 2012), the CICE5 interactive sea ice model (Bailey et al., 2018), and the Simple Land Interface Model (SLIM) (Laguë et al., 2019). Simulations are run at 2.5° resolution for 50 years, with the first 20 years discarded to allow for model spin-up. After 20 years, there is < 0.1 K drift in global mean surface temperatures (Fig. 1); the top of atmosphere energy imbalance in these near-equilibrium simulations is near-zero (≈0.3 W/m^2).

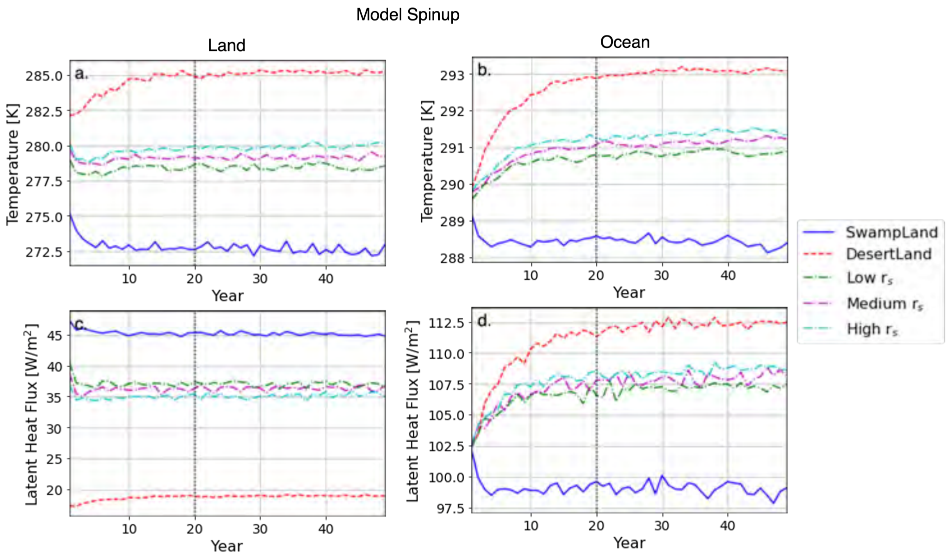

Figure 1. Annual mean, spatially averaged surface temperature (top) and latent heat flux (bottom) over land (left) and ocean (right) regions for the five CESM simulations explored in this study. Simulations have reached equilibrium prior to year 20.

The slab ocean has prescribed, seasonally and spatially varying pre-industrial ocean heat transport and heat capacity (slab or mixed-layer "depth") which is identical between simulations and from year-to-year within the same simulation. This allows sea surface temperatures to evolve in response to forcings, but does not allow for changes in ocean heat transport. The mixed-layer depth and heat transport values used in these simulations are calculated from the dynamic ocean component of the pre-industrial control simulation of the fully coupled CESM 1.2 model (as used in Garcia et al., 2016; Swann et al., 2018; Laguë et al., 2019). We use slab ocean values from a pre-industrial vs. present-day simulation because the pre-industrial climate is in equilibrium, while the ocean acts as a net energy sink in the present day climate. The ocean is a large source of variability in the Earth system, and the use of a slab ocean model allows us to focus on the atmospheric response to land surface changes, as the internal variability of the slab ocean model is small, allowing us to use a single simulation for each experiment rather than an ensemble. To explicitly demonstrate this, we run the initial 10 years of the two simulations described below ("SwampLand" and "DesertLand") with three ensemble members, each with initial land surface temperatures perturbed by $1e{-6}$ K; the spread between ensemble members is very small compared to the difference between the two experiments (Fig. S1). The default ocean albedo parameterization is used, where ocean albedo varies with solar declination, with default values of 0.06 for direct and 0.07 for diffuse radiation.

SLIM is used to allow us to directly control the physical properties of the land surface in a way that is difficult with complex land surface models. Hydrology is represented using a bucket model, with the resistance to evaporation calculated as a function of how much water is in the bucket as well as an additional user-prescribed resistance. A simple snow model allows for snow-albedo feedbacks on the land surface. The idealized land surface model allows us to artificially control terrestrial water availability without altering other aspects of the land surface. In contrast, if we were to override soil moisture in a complex land surface model like CLM5 (Lawrence et al., 2019), this would have follow-on impacts on leaf area, plant hydraulics, and the carbon cycle, which would in turn have follow-on impacts on albedo and surface evaporative resistance. In order to isolate the effect of surface water availability on climate, we need to leverage an idealized land surface model like SLIM.

We also want to test the response of the climate system to changes in land evaporation without cloud responses, which are a large source of model uncertainty. We could force clouds in CESM to be transparent to radiation, but this would lead to an unreasonably dark top of atmosphere albedo (unless we *also* modified surface albedo) and a much hotter base-state climate than CESM produces with the normal cloud parameterization. Instead, we conduct two additional simulations using Isca (Vallis et al., 2018), an idealized global circulation model which has radiatively interactive water vapor and produces precipitation, but where clouds are "invisible" to radiation in the standard, tested configuration. Simulations use a T42 grid, a slab ocean with a 20m mixed layer depth and prescribed modern heat transport, a bucket model for land hydrology with a heat capacity equal to that of a 2m ocean mixed layer, no snow albedo feedbacks, the modern continental configuration, realistic topography, and the RRTM radiation scheme (Clough et al., 2005). The albedo of the surface is set to be much higher than realistic values (0.25 for ocean and 0.325 for land), to generate a reasonable climate and top of atmosphere albedo (Thomson & Vallis, 2019; Geen et al., 2018).

2.2 Simulations

We consider five CESM simulations in this study, primarily focusing on two end-members of wet/dry land. Simulations have globally uniform land surface properties: all non-glaciated points on the land surface have the same albedo, aerodynamic roughness, capacity to hold water, and evaporative resistance. Glaciated gridcells (Greenland and Antarctica) have surface properties associated with ice, and do not vary between simulations (see Laguë et al., 2019, for details). The snow-free albedo of the land surface is set to 0.2 in visible wavelengths and 0.3 in the near-infrared, while the aerodynamic roughness is set to 0.1 m. While the base-state climate differs regionally in these simulations with globally uniform land surface properties compared to simulations with present-day land surface properties (see Laguë et al., 2019), we choose to use uniform, idealized land surface properties in order to isolate the sensitivity of the atmosphere to only the change in water availability at the land surface, without introducing the added dimension of imposing the difference in water availability onto different land surface types (e.g. land with different albedo).

In DesertLand, the first of our extreme simulations, the capacity of the land to hold water is reduced to 20 mm everywhere (compared to a typical value of ≈ 200 mm), and the resistance to evaporation is set to 100,000 s/m (compared to a typical value of ≈ 100 s/m); this effectively turns off evaporation from the land surface, regardless of precipitation or the atmospheric demand for water. DesertLand can physically be thought of as land free of vegetation with extremely well draining soils, such that all precipitation that falls on the land is quickly transferred into below ground aquifers or sub-surface runoff and returned to the oceans. In SwampLand, the second extreme simulation, the land surface is forced to be fully saturated with water at every time step. Land always has 200 mm of water available for evaporation, regardless of the precipitation or evaporation rates at each point. SwampLand can be thought of as land with a high water table and unlimited ground water supply. Physically, this is comparable to swampy regions on the modern land surface, but in this idealized simulation, these swamps are imposed over the entire non-glaciated land surface, regardless of elevation, slope, or distance from a water body.

Three additional simulations with interactive surface hydrology are also briefly considered, differing in their prescribed evaporative resistance: 30 s/m ("low" for low resistance), 100 s/m ("medium" for medium resistance), and 200 s/m ("high" for high resistance). Each simulation has the capacity to hold 200 mm of water at each non-glaciated land surface point, but the amount of water actually on the land surface is interactively simulated by the model based on precipitation and evaporation at each location.

Two additional simulations, similar to DesertLand and SwampLand, are conducted in the Isca model. In the DesertLand Isca simulation, the bucket capacity is set to 0.01 mm, while the bucket capacity in SwampLand is set to 150 mm and is "topped up" to always have 150 mm of water available at all land points at each time step.

2.3 Radiative Kernel

Changing surface evaporation between simulations alters atmospheric and surface temperatures, water vapor, cloud cover, and snow and ice extent. To isolate the individual contributions of each of these responses to the atmospheric energy budget, we use a radiative kernel for the CAM5 atmospheric model (Pendergrass et al., 2018) and follow the procedure introduced in Laguë, Swann, & Boos (2021), which we summarize here.

The radiative kernel provides the change in top-of-atmosphere (TOA) net shortwave and longwave radiation under both "full-sky" (including the effects of clouds) and "clear-sky" (without the effects of clouds) conditions that result from independent changes in the following quantities: surface albedo; surface temperature; air temperature at each level of the atmosphere; and specific humidity given a unit change in air temperature at constant relative humidity at each level of the atmosphere. The kernel also provides the change in downwelling shortwave and longwave radiation at the surface associated with each of these perturbations. Multiplying our simulated change in temperature, water vapor, etc. by the kernel returns the effect of that change on TOA or surface radiative fluxes.

We mask out differences in the stratosphere between simulations (as in Pendergrass et al., 2018; Shell et al., 2008), and multiply the water vapor kernel by the change in the natural logarithm of the simulated change in water vapor. We apply the clear-sky linearity test (Vial et al., 2013) to our most extreme simulations (SwampLand and DesertLand) and find generally excellent agreement between the change in TOA fluxes simulated by the full model and those predicted by the radiative kernel (Fig. 2). The exception is in the deep tropics, where the kernel and model are qualitatively similar, but disagree by a few W/m^2; these changes are primarily driven by disagreements in the tropical Atlantic and over tropical Africa (not shown). Note that all simulations here have a net input of energy into the TOA in the low latitudes and a net removal of energy from the TOA in the high latitudes under both clear-sky and full-sky conditions; Fig. 2 shows the *difference* in the TOA energy balance between two simulations. In the high latitudes, the positive values on this graph show that DesertLand is less negative than SwampLand, i.e. DesertLand is losing less energy at this latitude than SwampLand is. The negative values in the low latitudes show that DesertLand is less positive than SwampLand, i.e. that SwampLand is absorbing more total net energy into the Earth System at low latitudes compared to DesertLand. When we show results of calculations using the radiative kernel, any non-linearities or residuals in the radiative kernel are necessarily included in the cloud term; however, the excellent agreement in the clear-sky linearity test gives us confidence that such residuals are small.

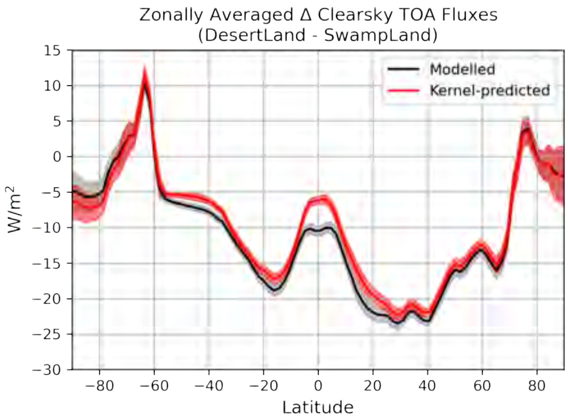

Figure 2. Zonal mean change (DesertLand - SwampLand) in TOA clear-sky radiation directly from the model (gray) and predicted by the clear-sky radiative kernel (red). Shading indicates $\pm 1\sigma$ of inter-annual standard deviation.

Analysis was conducted with the Python programming language, primarily with the NumPy (Harris et al., 2020) and xarray (Hoyer & Hamman, 2017) packages, using the JupyterHub (`https://jupyter.org/`) service on the Cheyenne computing system (Computational and Information Systems Laboratory, 2019). When statistical significance is shown on maps and vertical cross-sections, a value is deemed statistically significant if the p-values calculated from a Student's t-test pass a false discovery rate of 0.15 (following Wilks, 2016). Uncertainty intervals indicate $\pm 1\sigma$ of inter-annual standard deviation.

3 Results & Discussion

3.1 Column water vapor increases with suppressed land evaporation

As expected, SwampLand—the simulation with perpetually saturated land—has the largest terrestrial evaporation of the simulations considered, and the lowest average land surface temperatures (Fig. 3). In contrast, DesertLand—the simulation with perpetually suppressed land evaporation—has the lowest terrestrial evaporation (by design), and the warmest surface temperatures both on land and globally (Fig. 3a,b). The three simulations with intermediate values of terrestrial evaporative resistance lay between SwampLand and DesertLand in terms of evaporation, surface temperatures, and total atmospheric water vapor. There is a strong linear relationship across the simulations between terrestrial evaporation and terrestrial surface temperature, and between global mean surface temperatures and total atmospheric water vapor (Fig. 3c,d).

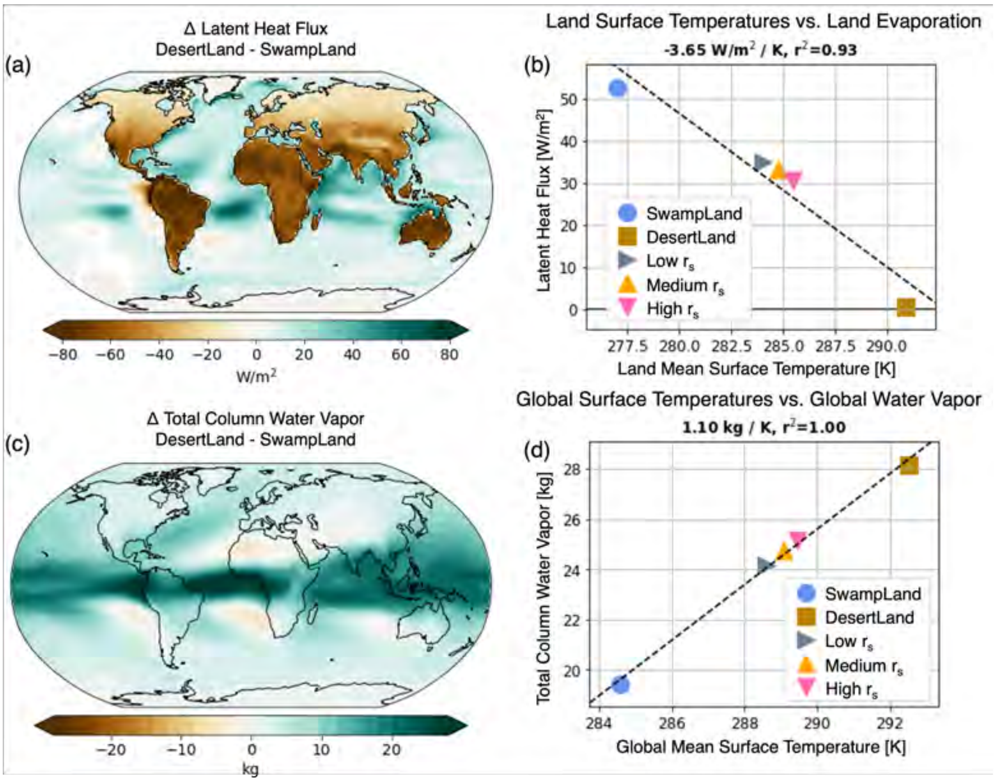

Figure 3. Annual mean change in latent heat flux (a) and total column water vapor (c) for the DesertLand - SwampLand simulations. Scatter plots showing the relationship between annual mean (b) land surface temperature and terrestrial evaporation and (d) global mean surface temperature and global mean total column water vapor. In a/c, only changes that pass a statistical test are shown, where values are significant if the p-values calculated from a student's t-test pass a false discovery rate of 0.15.

DesertLand has the most atmospheric water vapor, despite having suppressed land evaporation (Figs. 3). The planet as a whole is not water limited in the modern continental configuration, so ocean evaporation increases in the DesertLand simulation (Fig. 4a). However, this only partially compensates for the reduction in land evaporation, so there is less surface evaporation in the global mean in DesertLand. Precipitation over both land and ocean is accordingly reduced in DesertLand, but the atmosphere has more total water vapor in DesertLand than SwampLand (Fig. 4c). This is true of both land and ocean regions in the lower and upper troposphere, except for a drying of some subtropical regions and in the lower troposphere of inland continental regions (Figs. 5, 6).

The reduction in global mean precipitation and increase in global mean water vapor content together imply an increase in the residence time of atmospheric water vapor. Specifically, this residence time has been defined as the ratio of global mean precipitable water Q to global mean precipitation P (Trenberth, 1998),

$$\tau \equiv \frac{Q}{P} \tag{1}$$

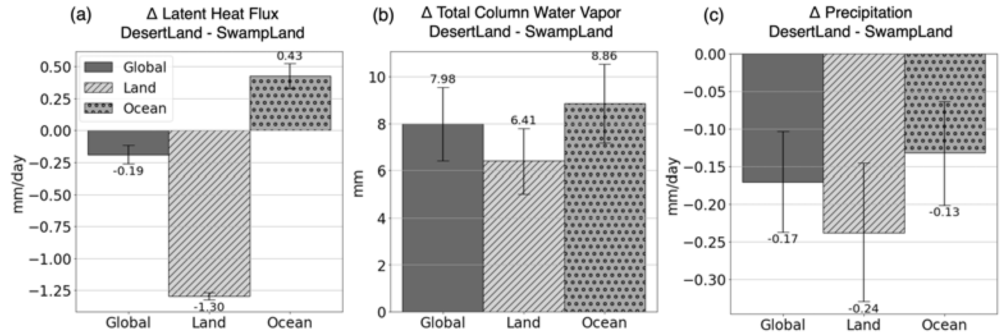

Figure 4. Annual mean change (DesertLand - SwampLand) in area-weighted mean (a) latent heat flux [mm/day], (b) column water vapor [mm], and (c) precipitation [mm/day], separated into the global (solid), land (hatched), and ocean (dotted) contributions. Error bars indicate $\pm 1\sigma$ of inter-annual standard deviation. Note that as there is more ocean than land area, bars within each subplot do not sum directly.

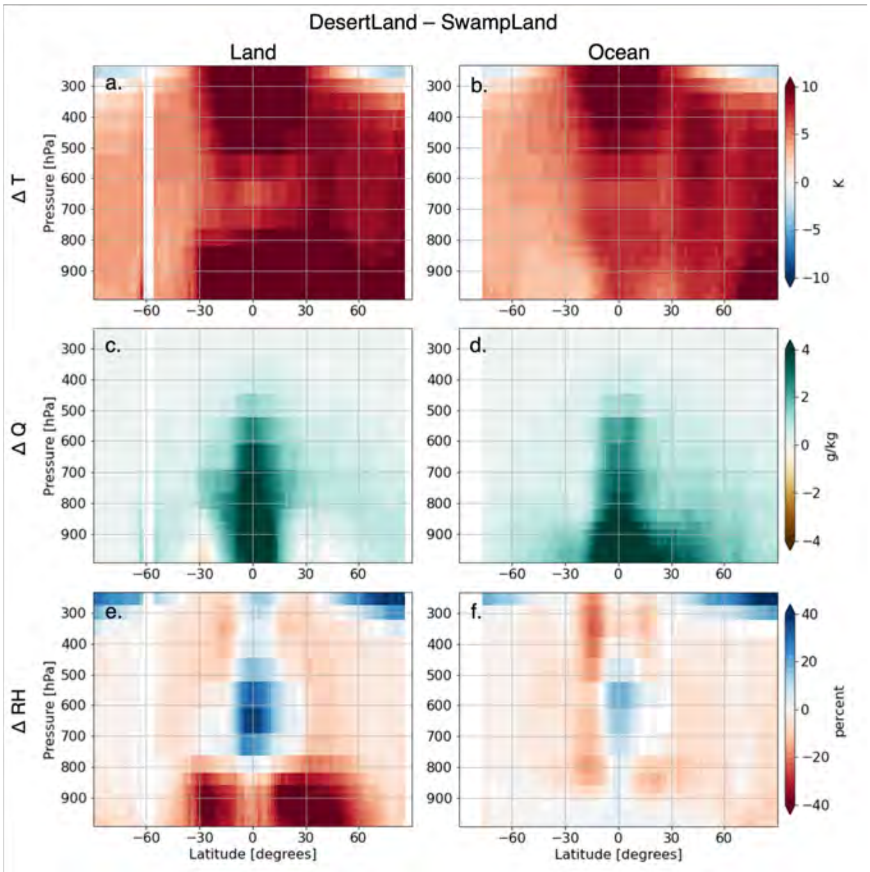

Figure 5. Zonal mean vertical cross sections of the change in temperature (T [K], top), specific humidity (Q [g/kg], middle), and relative humidity (RH [%], bottom) over land regions (left) and ocean regions (right). Only changes that pass a statistical test are shown, where values are significant if the p-values calculated from a student's t-test pass a false discovery rate of 0.15.

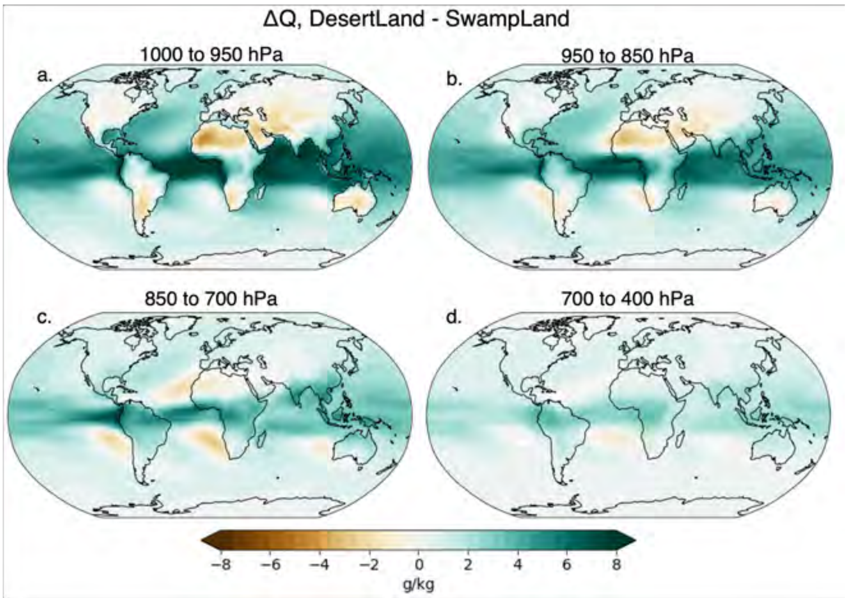

Figure 6. Change (DesertLand - SwampLand) in specific humidity [g/kg] from (a) 1000-950 hPa, (b) 950-850 hPa, (c) 850-700 hPa, and (d) 700-450 hPa. Only changes that pass a statistical test are shown, where values are significant if the p-values calculated from a student's t-test pass a false discovery rate of 0.15.

Here we find that τ increases from 6.7 days in SwampLand to 10.2 days in DesertLand. One may alternatively interpret this change as a reduction in the convective mass flux that transports water vapor vertically until it condenses and precipitates (Held & Soden, 2006). Thus, while a reduction in land evaporation is expected to produce a transient reduction in local atmospheric water vapor, changes in the precipitating atmospheric circulation dominate to allow more water to accumulate in the atmosphere and then be maintained at that higher level. Locally, water vapor over land is maintained by a balance between local evaporation, local precipitation, and the convergence of water by large-scale winds; the latter two are typically large compared to the former, making possible indirect effects of a surface evaporative forcing. Furthermore, Sun & Wang (2022) found a reduction in precipitation intensity in hot weather in moisture limited regions (e.g. over land) as a result of an increased saturation deficit.

3.2 Cloud feedbacks enhance energy input over land

We now describe how suppression of surface evaporation produces a reduction in low cloud cover (Fig. 7), increasing the energy absorbed by land and the precipitating large-scale circulation driven by that energy source. Reductions in cloud cover driven by suppressed terrestrial evaporation lead to an additional $\approx$37 W/m^2 of shortwave radiation absorbed by the surface (Fig. 8). The largest reductions occur in low clouds over land, and are thus consistent with a local response to the land evaporative forcing. The reduced cloud cover also makes it easier for longwave radiation emitted by land to exit the top of the atmosphere, but this is smaller in magnitude than the shortwave cloud effect (as expected given the low altitude of the cloud changes), yielding a net positive heating of land by cloud radiative effects of about 11 W/m^2. Other components of the surface energy budget are discussed below, when we use the model's radiative kernel to decompose the net change into different physical components.

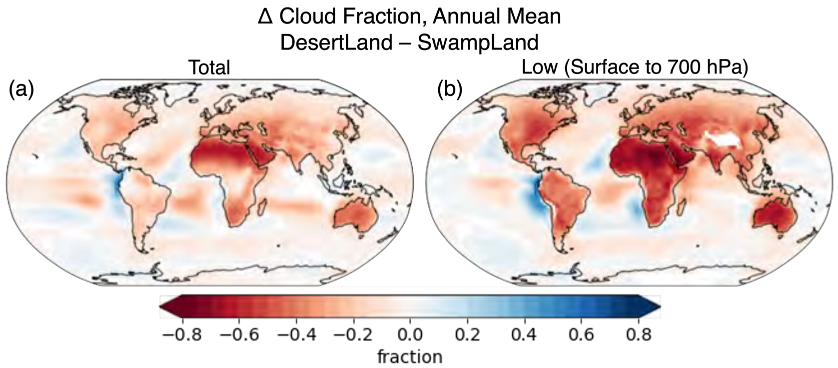

Figure 7. Annual mean change (DesertLand - SwampLand) in total cloud fraction (left) and low cloud fraction (right) for the CESM simulations. Only changes that pass a statistical test are shown, where values are significant if the p-values calculated from a student's t-test pass a false discovery rate of 0.15.

Reductions in low cloud cover over land as a result of suppressing terrestrial evaporation also impact the TOA energy budget (Fig. 9). In particular, loss of low cloud cover over land lowers the planetary albedo; this results in more energy absorbed at the TOA and in turn should increase global mean temperatures. Increased temperatures should, in turn, lead to an increase in water vapor following the Clausius-Clapeyron relationship. That is, the reduction in low cloud cover alone should lead to increased atmospheric temperatures and water vapor. Without the reduction in low cloud cover, suppressing terrestrial evaporation would not necessarily lead to any increased energy into the Earth system at the top of the atmosphere, and would lead to weaker warming at the surface as the only warming mechanism would be the reduction in latent cooling, with no additional warming from increased solar radiation due to reduced cloud cover. Indeed, we see this later when we conduct similar simulations in a model without cloud cover.

We roughly estimate the effect of the change in clouds on global mean temperatures and water vapor as follows: in the global mean, the change in clouds leads to a 12.8 W/m^2 increase in energy into the Earth system at the TOA (14.8 W/m^2 from shortwave radiation, -2 W/m^2 from longwave radiation; Fig. 9). Using a climate response parameter of 1.5 $W/m^2/K$ (from Gregory (2004)'s estimates for increased TOA insolation), this would result in a roughly 8.5 K temperature increase, close to the actual global mean temperature increase in our simulations of roughly 8 K (from a global mean of 283.5 to 291 K; Fig. 3d). Assuming that column water vapor scales with surface air temperature at a rate of roughly 7%/K per the Clausius-Clapeyron relationship (O'Gorman & Muller, 2010b; Held & Soden, 2006), we would expect water vapor to increase roughly 70% (the Clausius-Clapeyron equation is exponential, so the relative increase in saturation vapor pressure for the relatively large warming of 8 K is substantially larger than the infinitesimal rate of change of 7%/K); the actual increase in total atmospheric water vapor in our simulations was roughly 40% (from a global mean of 19 to 28 kg; Fig. 3d), with reductions in tropical lower-tropospheric relative humidity over land that peak near -40% (Fig. 5e). Thus, this simple argument provides similar order of magnitude changes in temperatures and water vapor as our full simulations, but with a nearly factor-of-two overestimate in the vapor increase because the radiative forcing (a reduction in low clouds) is driven by lower-tropospheric drying. We note that there is a lot of uncertainty in the value of the climate response parameter, both across models and across forcing mechanisms (e.g. CO_2, insolation, etc.) within a single model (Gregory, 2004; Hansen et al.,

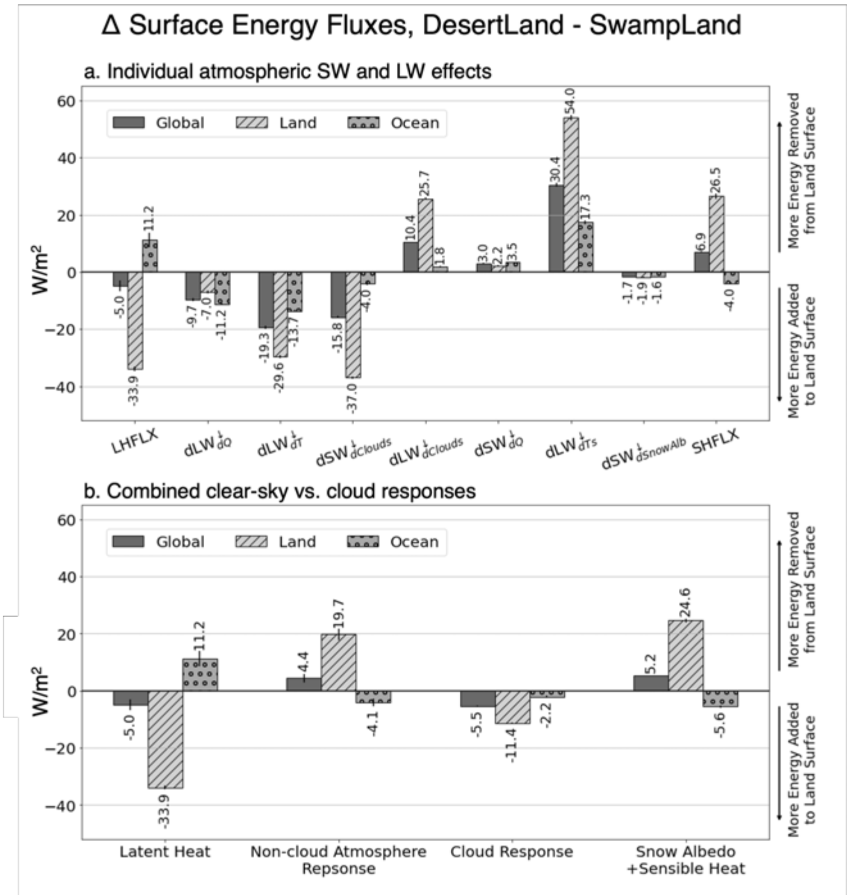

Figure 8. Change in global (solid), land (hatched), and ocean (dotted) annual mean surface fluxes for DesertLand - SwampLand. The breakdown of surface flux changes due to latent (LHFLX) and sensible (SHFLX) heat, and shortwave (SW) and longwave (LW) radiation are shown. Panel (a) shows the changes in surface shortwave and longwave radiative fluxes decomposed using the radiative kernel into the contributions due to water vapor, atmospheric temperatures, surface temperatures, cloud cover, and surface albedo (i.e. snow changes), as well as the changes due to latent and sensible heat. Panel (b) combines the fluxes into those driven by latent heat flux, the cloud-free atmosphere and Plank response (air temperature, water vapor, and surface temperature), those driven by clouds, and other surface changes (sensible heat flux, albedo). The inter-annual standard deviation is marked by the vertical black lines capping each bar. Downwards (negative) values indicate that the change in the flux leads to more energy into the land surface (i.e. a warming effect), while upwards (positive) values indicate less energy into the land surface or more energy removed from the land surface.

1997), and that 7%/K is not an exact Clausius-Clapeyron scaling (O'Gorman & Muller, 2010b).

3.2.1 Decomposing the energy balance with a radiative kernel

The increase in near-surface MSE is driven by a combination of factors. In the absence of evaporative cooling (i.e. the DesertLand simulation), changes in the atmosphere which increase radiative fluxes into the land surface necessarily lead to warming. Over land, suppressed terrestrial evaporation directly increases the energy that must be removed from the surface as sensible heat or longwave radiation (Fig. 8, spatial patterns shown in Fig. S2). Reducing evaporation results in excess energy available in the land surface (≈34 W/m^2 averaged over all land areas). The increase in energy into the land surface from increase downwelling longwave radiation as a result of suppressed land evaporation (29.6 W/m^2 from air temperatures and an additional 7 W/m^2 from increased water vapor) is of a similar magnitude to the increase in energy into the land surface from suppressed latent heat flux (33.9 W/m^2).

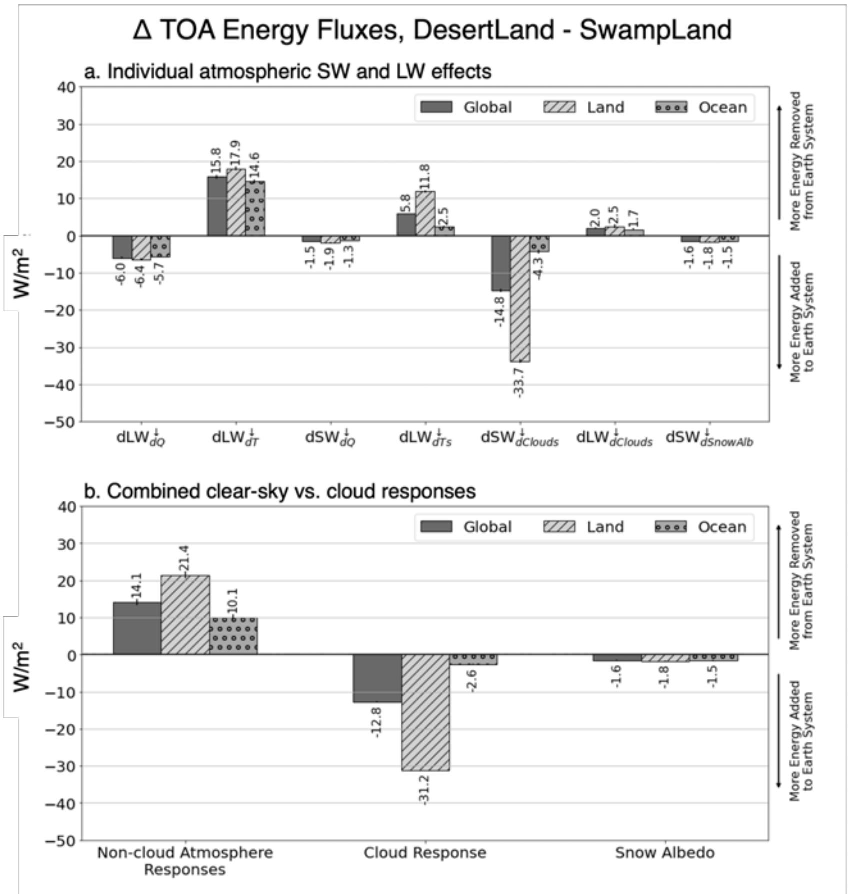

Figure 9. Change in global (solid), land (hatched), and ocean (dotted) annual mean top of atmosphere (TOA) fluxes for DesertLand - SwampLand. The breakdown of toa flux changes due to shortwave (SW) and longwave (LW) radiation are shown. Panel (a) shows the changes in toa shortwave and longwave radiative fluxes decomposed using the radiative kernel into the contributions due to water vapor, atmospheric temperatures, surface temperatures, cloud cover, and surface albedo (i.e. snow changes). Panel (b) combines the fluxes into those driven by the cloud-free atmosphere and Plank response (air temperature, water vapor, and surface temperature), those driven by clouds, and surface albedo. The inter-annual standard deviation is marked by the vertical black lines capping each bar. Downwards (negative) values indicate changes that lead to more energy absorbed by the Earth system at the TOA while upwards (positive) values indicate energy removed from the Earth system at the TOA.

The longwave effects of increased water vapor act against the negative longwave cloud effect (Figs. 8, S2b,d). Increased water vapor itself drives a feedback on the surface energy balance, with more water vapor leading to more longwave radiation into the surface (7.9 W/m^2); this term is of comparable magnitude to (though slightly smaller than) net cloud radiative effects (11.4 W/m^2) over land; Figs. 8, S2). Previous work has shown how changes in terrestrial evaporation modulate the water vapor greenhouse effect; specifically, Laguë, Pietschnig, et al. (2021) show that while reducing land evaporation directly warms the surface, over very large idealized continents, reductions in land evaporation lead to reduced atmospheric water vapor and drive an overall cooling at the surface by reducing the water vapor greenhouse effect. In this study (with the modern Earth's continental configuration), our results show that land's control on water vapor is still an important contribution to the radiation budget, with the changes in surface and TOA fluxes driven by changes in water vapor of comparable magnitude to the combined shortwave and longwave effects of changes in cloud cover.

The combined effect of atmospheric responses to suppressed terrestrial evaporation is a slight increase in longwave energy into the surface, and a larger increase in shortwave radiation into the surface which, over land areas, is comparable in magnitude to the increase in surface energy coming from reduced latent cooling. Suppressing terrestrial evaporation leads to a net radiative flux of roughly 6 W/m^2 out of the land surface (the sum of all the radiative fluxes in Fig. 8a), which is balanced by the combined changes in sensible and latent heat flux. While increased sensible heat flux (associated with higher surface temperatures in DesertLand vs. SwampLand) increases energy removed from the surface (by 26.5 W/m^2 over land), suppressed latent heat flux over land means 33.9 W/m^2 of energy is not removed from the land surface through evaporation. The response of the radiative terms of the surface energy budget over the oceans are of the same sign as the changes over land, though of different magnitude. In contrast, because ocean evaporation increases when terrestrial evaporation is suppressed, this removes energy from the surface, balanced by reductions in sensible heat flux. Over land areas, the radiative effects of cloud changes are larger than the combined radiative effects of water vapor and temperature changes (Fig. 8b).

The importance of the cloud feedback is reinforced by considering the change in top of atmosphere (TOA) energy fluxes. The shortwave effects of reductions in cloud cover in DesertLand-SwampLand are the single largest contributor to changes in the top of atmosphere energy balance over land (Fig. 9, spatial patterns in Fig. S3; the largest cloud reductions occur in low clouds over land areas (Fig. 7). The difference between the TOA and surface energy flux anomalies is the anomalous net energy input (NEI) to the atmosphere discussed below. Both the DesertLand and SwampLand simulations are in equilibrium, so the net TOA energy balance (the sum of the bars in Fig. 9) is near zero.

3.2.2 Enhanced energy sources drive tropical ascent

The reduction in low clouds in the Desertland vs. SwampLand simulation lead to an increase in the total amount of solar energy absorbed at the land surface—energy which is then emitted back to the atmosphere through the surface energy budget. Specifically, suppressed terrestrial evaporation leads to an increase over most land regions in the net energy input to the atmosphere (NEI), which is the sum of radiative and surface turbulent fluxes into the atmosphere through its top and bottom boundaries (Fig. 10d). It also leads to an increase in near-surface moist static energy (MSE) over most continental regions, especially in the tropics (Fig. 11). We calculate moist static energy as

$$MSE = c_pT + L_vQ + gZ, \tag{2}$$

the sum of the dry energy (the heat capacity c_p of dry air multiplied by the air temperature T), potential energy (the gravitational constant of acceleration g multiplied by the geopoential height Z), and the moist energy (the latent heat of vaporization L_v multiplied by water vapor Q) of a static (non-dynamic) parcel of air. Note that while we show the NEI for clear-sky CESM, the latent and sensible heat fluxes which go into the NEI calculation are from the full CESM model that includes cloud effects on the surface energy budget; as such, Fig. 10e should be treated with appropriate caution.

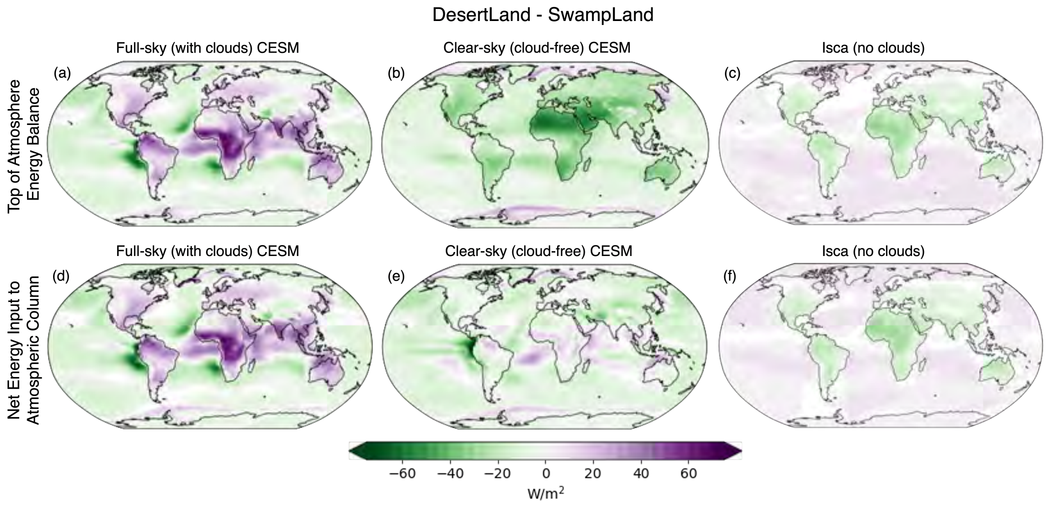

Figure 10. Annual mean change (DesertLand - SwampLand) in the top of atmosphere energy budget (net shortwave - outgoing longwave radiation; top row) and net energy input (NEI: net top of atmosphere - net surface fluxes; bottom row). The full CESM simulation, including cloud radiative effects, is shown in the left column; CESM where radiative fluxes ignore the influence of clouds ("clear-sky" conditions) are shown in the centre column, while Isca, which is always radiatively cloud-free, is shown in the right column. Only changes that pass a statistical test are shown, where values are significant if the p-values calculated from a student's t-test pass a false discovery rate of 0.15.

Two complementary theoretical frameworks can then help in understanding the response of the large-scale circulation to our surface evaporative forcing. First, by vertically integrating the moist static energy budget, one can relate large-scale vertical winds to the local input of energy through the top and bottom boundaries of the atmosphere,

$$-\omega_1 M = NEI \tag{3}$$

where ω_1 is the vertical motion at a characteristic level, and M is a coefficient known as the gross moist stability (Neelin & Held, 1987; Sobel et al., 2007; Raymond et al., 2015). Being a measure of the vertical energy stratification of the atmosphere, M is typically positive in the time mean in deep-convecting regions, expressing the fact that time-mean ascent typically exports energy from the column in many tropical regions. Thus, the increase in NEI due to reduced low cloud cover is accompanied by enhanced large-scale ascent in many tropical land regions (Figs. 12a, S4). While this anomalous ascent is bottom-heavy, it extends the full depth of the troposphere. There is an increase in precipitation over many of the regions in which there is an increase in NEI (Fig. 12b). Outside of the tropics, precipitation over land decreases (Fig. 12b). Though there is increased time-mean upwards motion and increased NEI (Fig. S5), this does not lead to more precipitation, consistent with the fact that precipitation there is generated primarily by the moisture converged by transient motions, rather than time-mean flow.

In an alternate framework, one can consider the energy content of air (MSE) instead of the source of atmospheric energy (the NEI); precipitating ascent in the low-latitude atmosphere generally lies near the maximum in surface air MSE and increases in intensity with horizontal gradients in that MSE. This is expected when surface air MSE is

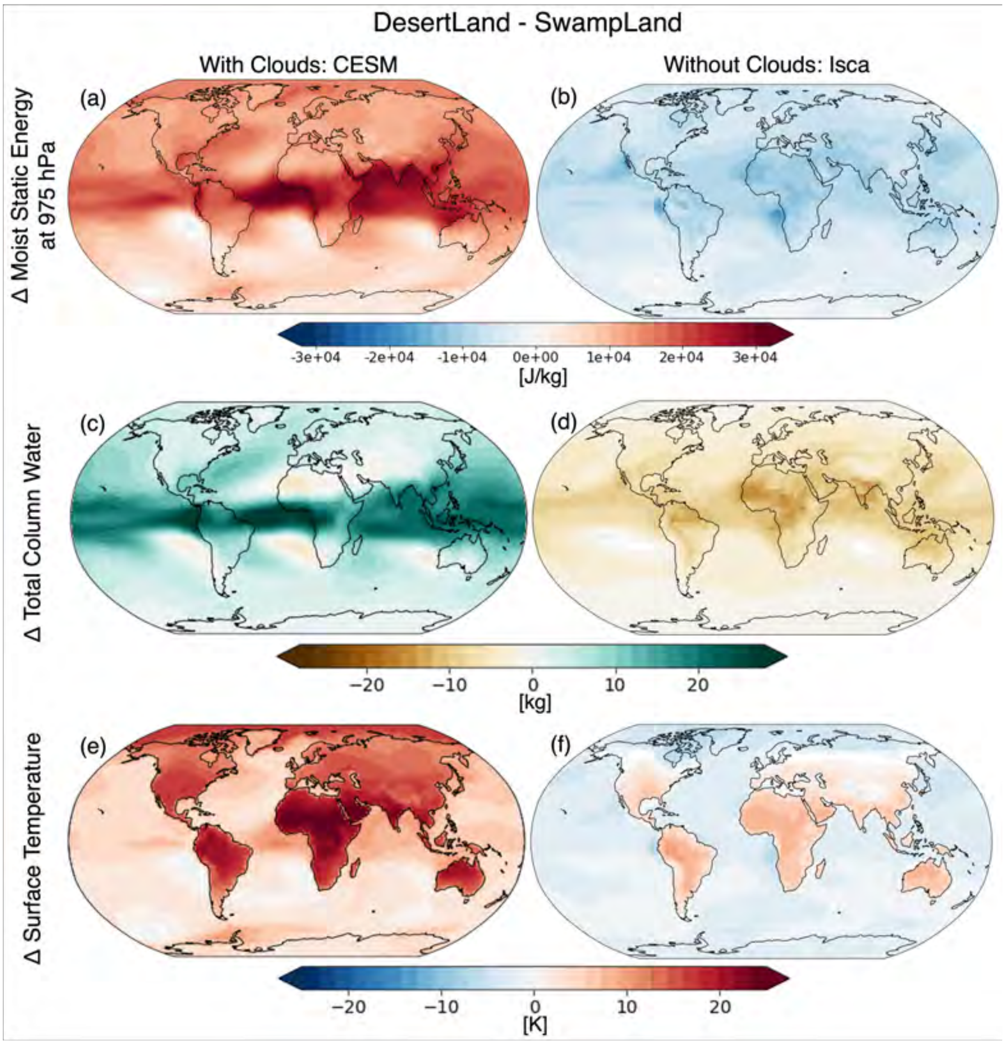

Figure 11. Annual mean change (DesertLand - SwampLand) in near-surface (975 hPa) moist static energy (top), total column water vapor (middle), and surface temperature (bottom) for CESM (left) and Isca (right) simulations. Only changes that pass a statistical test are shown, where values are significant if the p-values calculated from a student's t-test pass a false discovery rate of 0.15.

convectively coupled to free-tropospheric temperatures (Emanuel et al., 1994; Neelin, 2007; Privé & Plumb, 2007; Shekhar & Boos, 2016), and has been shown to describe the observed tropical climatology and interannual variability (Nie et al., 2010; Hurley & Boos, 2013). Suppressed surface evaporation increases MSE (because of the atmospheric feedbacks discussed above), particularly over tropical regions which thus enhances the magnitude of the meridional gradient in MSE, and in turn the large-scale tropical overturning circulation (Fig. 11a, 12). Decreases in moisture in the lower atmosphere over most land areas (driven by reduced surface evaporation) would lead to a reduction in MSE, but this is more than compensated for by increases in temperatures, which lead to an overall increase in MSE at 975 hPa over land areas (Fig. S6); changes in geopotential heights are negligible.

Neither of these frameworks provides a closure for the amount of water vapor in the atmosphere, but in Earth's low-latitude atmosphere, where most water vapor lies and where horizontal temperature gradients are weak, MSE generally scales like precipitable water (Charney, 1963; Sobel et al., 2001) given the general availability of the ocean water supply in the modern continental configuration. In other words, large-scale ascent will advect water vapor upward, humidifying the column over land regions despite suppressed terrestrial evaporation. The MSE increase aloft over land in DesertLand indeed consists of increases in both temperatures and specific humidities (specific humidity decreases near the surface, but increases aloft), though the latter increase slowly enough that RH over land decreases (Fig. 5e); the increases in relative humidity occurring near the poles at high altitudes occur in the stratosphere and are not considered in this study (indeed, changes in T and Q above the tropopause are masked out of all calculations involving the radiative kernel, as in Pendergrass et al. (2018); Shell et al. (2008); Laguë, Swann, & Boos (2021)). While the warming in our simulations is driven by changes in land evaporation, for CO_2-driven warming, Byrne & O'Gorman (2016) also find near-surface continental relative humidity decreases. In simulations of future climate, we would expect both the radiative effects of CO_2 as well as changes in terrestrial evaporation to drive changes in atmospheric moisture. The only terrestrial regions where total column water vapor decreases is in the dry subtropics (e.g. the Sahara) where subsidence increases (Figs. S4, S5).

The discussion above differs greatly from arguments in which continental water vapor is treated as being set by transport from ocean regions. Anomalous near-surface winds do bring moist ocean air onto tropical land in DesertLand vs. SwampLand, e.g. in tropical South America, Africa, and Asia (Fig. 12b). However, such onshore winds need not produce ascent that spans most of the depth of the troposphere. Strong land-sea temperature gradients, such as those between a desert and ocean on Earth, often produce shallow, non-precipitating circulations; we will show below that, without cloud-radiative effects, suppressed land evaporation indeed leads to enhanced onshore flow that is shallow, non-precipitating, and that does not result in enhanced total column water vapor.

3.2.3 The response without cloud-radiative effects

When similar "desert" and "swamp" simulations are repeated with a cloud-free idealized global circulation model (Isca), surface temperatures still increase in response to suppressed terrestrial evaporation (Fig. 11f). However, both near-surface MSE (Fig. 11b) and atmospheric water vapor over continental regions (Fig. 11d) decrease. Unlike the CESM simulations, where the reduction in low cloud cover leads to an increase in energy into the Earth system at the top of the atmosphere, the Isca simulations do not have this additional energy source to the system as there are no clouds.

Suppressing terrestrial evaporation leads to a decrease in the atmospheric NEI and the net top of atmosphere energy budget over continents in the Isca simulations (Fig. 10). While the Isca simulations still show some anomalous upward motion over the continents in the lower atmosphere, and near-surface onshore flow from the oceans to the land in many regions (Figs. S7 & S8), these are shallow, non-precipitating anomalous circulations that contrast strongly with the deep, precipitating anomalous flow in CESM (c.f. S4 & S7). Similarly, the warming induced by suppressed terrestrial evaporation in Isca is restricted to the near-surface atmosphere over land regions, while CESM warms throughout the column (c.f. Fig. 5 & S9). While there are many differences between CESM and Isca, a key difference in the response to altered terrestrial evaporation is the response of cloud cover, which CESM includes and Isca does not. This highlights the importance of understanding cloud feedbacks—already a large source of climate uncertainty (Zelinka et al., 2017)—for determining how terrestrial evaporation changes alter the climate system.

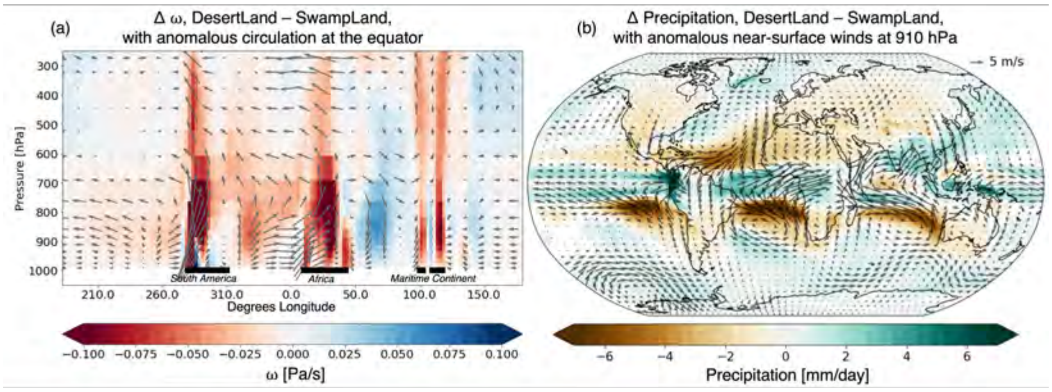

Figure 12. (a) Vertical cross section (longitude vs. pressure) at the equator for the change in vertical motion ω [Pa/s] for DesertLand − SwampLand is shown in colors, with red indicating negative ω, i.e. positive vertical motion. Vectors show the direction of anomalous motion: u winds in [m/s] in the x-direction, and $\omega \times -150$ in [Pa/s] in the y direction. ω is multiplied by -1 so arrows point in the direction of motion, and by 150 as an arbitrary scaling such that the vertical component is of comparable magnitude to the horizontal component, for ease of visualization. Horizontal black lines at the surface indicate land masses. (b) Change in precipitation (shading) for DesertLand − SwampLand, with vectors showing anomalous $\langle u, v \rangle$ winds [m/s] at 910 hPa. Only changes that pass a statistical test are shown, where values are significant if the p-values calculated from a student's t-test pass a false discovery rate of 0.15.

While we do not have a CESM simulation without radiatively interactive clouds, we can crudely compare the radiative fluxes in the Isca simulations to the top of atmosphere radiative fluxes calculated using "clear-sky" conditions in CESM (Fig. 11b/e). The clear-sky fluxes are calculated at each time step ignoring the radiative effects of clouds; however the model is integrated forwards using the full sky (including the radiative effects of clouds) fluxes—that is, the temperature, moisture, dynamics, etc. of CESM are consistent with the full-sky radiative fluxes, not the clear-sky radiative fluxes. Both the clear-sky CESM simulations and the Isca simulations show a decrease in the TOA energy balance over land regions when terrestrial evaporation is suppressed, reflecting the fact that the increase in energy into the Earth system in the CESM simulations are due to changes in low cloud cover over land.

While both CESM and Isca allow us to test the response of the climate system to suppressed terrestrial evaporation, we note that there are limitations in comparing results between these two models, as they do not provide an apples-to-apples comparison. In future work, a perhaps more robust comparison would be to compare the full CESM-SLIM model to a version of CESM where the clouds have been modified to be transparent to radiation; however, this model would produce unrealistically high TOA albedos, thus an increase in the surface albedo (such as is done in Isca) would be necessary to replicate a similar climate to the modern Earth. Such a modified model configuration would need to be evaluated and benchmarked before using it for this kind of experiment. Similarly, a modified version of Isca that included radiatively interactive clouds could also be leveraged to understand interactions between terrestrial evaporation, cloud cover, and the global energy budget. In this study however, we present the results of both the CESM and Isca simulations as complimentary; both indicate a strong control of terrestrial evaporation on surface climate, and the model that allows for interactive cloud changes (CESM) suggests further investigation of the coupling of terrestrial evaporation and cloud cover is of merit. Additionally, we note that all the simulations shown in this study are highly idealized; they are useful for improving our mechanistic understanding of interactions between terrestrial processes and global climate, and can be used to inform more realistic studies of the effects of changes in terrestrial evapotranspiration driven by vegetation change, land use, agriculture, climate change, etc. on global climate.

4 Conclusions

In a global model with realistic continental geometry, reducing terrestrial evaporation increases the total amount of atmospheric water vapor over most land and ocean regions. The residence time of water vapor in the atmosphere increases by roughly 50% from the simulation with fully saturated land to the simulation with desert land. Suppressing land evaporation has a direct warming effect on the land surface by reducing latent cooling of the surface, but also drives atmospheric feedbacks including reductions in terrestrial cloud cover. The anomalous surface energy fluxes driven by atmospheric cloud, water vapor, and temperature feedbacks are larger than the initial change in latent heat flux driven directly by suppressed terrestrial evaporation. The cloud feedback is critical for increasing near-surface moist static energy and generating anomalous atmospheric circulations throughout the depth of the troposphere. Simulations conducted in a cloud-free model still show surface warming with suppressed terrestrial evaporation, but also show a decrease, rather than an increase, in near surface MSE. Anomalous atmospheric circulations over the continents in cloud-free simulations are much shallower, and the atmosphere shows reduced atmospheric water vapor with suppressed terrestrial evaporation. This extreme experiment raises the question of how real-world changes to the land surface (e.g. land use, agriculture) may be contributing to climate change by altering atmospheric water vapor and cloud cover, and how terrestrial evaporation modulates climate on other planets or in past continental configurations of Earth's history.

Data Availability Statement

Source code for the models used are publicly available on github at `https://github.com/marysa/SimpleLand/releases/tag/slim0.1.006_release-cesm2.1.4` for SLIM, `https://github.com/ESCOMP/CESM/releases/tag/release-cesm2.1.1` for CESM, and `https://github.com/ExeClim/Isca/releases/tag/v1.0` for Isca. The specific versions used in this study are archived on zenodo in the following locations: SLIM, at `https://zenodo.org/badge/latestdoi/509227365` (DOI: 10.5281/zenodo.7352717); CESM, at `https://doi.org/10.5281/zenodo.3895315` (DOI: 10.5281/zenodo.3895315); and Isca, at `https://github.com/ExeClim/Isca/releases/tag/v1.0`, respectively. The modified version of Isca used in this study is available via zenodo at `https://doi.org/10.5281/zenodo.6800218`. Output from the simulations, analysis scripts, and model setup files used in this study are available on Zenodo at `https://doi.org/10.5281/zenodo.7909213`).

Author Contributions Statement

MML developed the idea for the study, modified the models, performed the simulations, and conducted the analysis. All authors discussed the experimental design and results. MML wrote the initial draft and all authors contributed to the manuscript.

ORCID iDs

Marysa M Laguë: https://orcid.org/0000-00018513-542X
Gregory R Quetin: https://orcid.org/0000-00027884-5332
William R Boos: https://orcid.org/0000-00019076-3551

Acknowledgments

We acknowledge high-performance computing support from Cheyenne (doi:10.5065/D6RX99HX) provided by NCAR's Computational and Information Systems Laboratory, sponsored by the National Science Foundation. M.M.L. acknowledges funding support from the James S. McDonnell Foundation Postdoctoral Fellowship in Dynamic and Multiscale Systems.

References

Bailey, D., Hunke, E., DuVivier, A., Lipscomb, B., Bitz, C., Holland, M., ... Schramm, J. (2018). *CESM CICE5 Users Guide* (Tech. Rep.).

Ball, J. T., Woodrow, I. E., & Berry, J. A. (1987). A Model Predicting Stomatal Conductance and Its Contribution to the Control of Photosynthesis Under Different Environmental Conditions. *Progress in Photosynthesis Research*(January). doi: 10.1007/978-94-017-0519-6

Berg, A., Findell, K., Lintner, B., Giannini, A., Seneviratne, S. I., Van Den Hurk, B., ... Milly, P. C. D. (2016). Land–atmosphere feedbacks amplify aridity increase over land under global warming. *Nature Climate Change*, *6*(May), 869–874. doi: 10.1038/nclimate3029

Bonan, G. B. (2008). *Ecological Climatology.* Cambridge Univ. Press, Cambridge, UK.

Boos, W. R., & Korty, R. L. (2016). Regional energy budget control of the intertropical convergence zone and application to mid-Holocene rainfall. *Nature Geoscience*, *9*(12), 892–897. doi: 10.1038/ngeo2833

Budyko, M. I. (1961). The Heat Balance of the Earth's Surface. *Soviet Geography*, *2*(4), 3–13. doi: 10.1080/00385417.1961.10770761

Byrne, M. P., & O'Gorman, P. A. (2015, October). The Response of Precipitation Minus Evapotranspiration to Climate Warming: Why the "Wet-Get-Wetter, Dry-Get-Drier" Scaling Does Not Hold over Land*. *Journal of Climate*, *28*(20), 8078–8092. doi: 10.1175/JCLI-D-15-0369.1

Byrne, M. P., & O'Gorman, P. A. (2016). Understanding decreases in land relative humidity with global warming: Conceptual model and GCM simulations. *Journal of Climate*, *29*(24), 9045–9061. doi: 10.1175/JCLI-D-16-0351.1

Charney, J. G. (1963, November). A Note on Large-Scale Motions in the Tropics. *Journal of the Atmospheric Sciences*, *20*(6), 607–609. doi: 10.1175/1520-0469(1963)020⟨0607:ANOLSM⟩2.0.CO;2

Clough, S. A., Shephard, M. W., Mlawer, E. J., Delamere, J. S., Iacono, M. J., Cady-Pereira, K., ... Brown, P. D. (2005). Atmospheric radiative transfer modeling: A summary of the AER codes. *Journal of Quantitative Spectroscopy and Radiative Transfer*, *91*(2), 233–244. doi: 10.1016/j.jqsrt.2004.05.058

Collins, M., Knutti, R., Arblaster, J., Dufresne, J. L., Fichefet, T., Friedlingstein, P., ... Wehner, M. (2013). Long-term climate change: Projections, commitments and irreversibility. *Climate Change 2013 the Physical Science Basis: Working Group I Contribution to the Fifth Assessment Report of the Intergovernmental Panel on Climate Change*, *9781107057*, 1029–1136. doi: 10.1017/CBO9781107415324.024

Computational and Information Systems Laboratory. (2019). *Cheyenne: HPE/SGI ICE XA System (University Community Computing).* Boulder, CO: National Center for Atmospheric Research. doi: 10.5065/D6RX99HX

Davin, E. L., de Noblet-Ducoudré, N., de Noblet-Ducoudre, N., & de Noblet-Ducoudré, N. (2010, January). Climatic Impact of Global-Scale Deforestation: Radiative versus Nonradiative Processes. *Journal of Climate*, *23*(1), 97–112. doi: 10.1175/2009JCLI3102.1

Dirmeyer, P. A. (1994). Vegetation Stress as a Feedback Mechanism in Midlatitude Drought. *Journal of Climate*, *7*.

Dirmeyer, P. A. (2006). The hydrologic feedback pathway for land-climate coupling.

Journal of Hydrometeorology, *7*(5), 857–867. doi: 10.1175/JHM526.1
Dirmeyer, P. A. (2011). The terrestrial segment of soil moisture-climate coupling. *Geophysical Research Letters*, *38*(16), 1–5. doi: 10.1029/2011GL048268
Donohue, R. J., Roderick, M. L., McVicar, T. R., & Farquhar, G. D. (2013). Impact of CO2 fertilization on maximum foliage cover across the globe's warm, arid environments. *Geophysical Research Letters*, *40*(12), 3031–3035. doi: 10.1002/grl.50563
Eltahir, E. A., & Bras, R. L. (1996). Precipitation Recycling. *Reviews of Geophysics*(96), 367–378.
Emanuel, K. A., David Neelin, J., & Bretherton, C. S. (1994, July). On large-scale circulations in convecting atmospheres. *Quarterly Journal of the Royal Meteorological Society*, *120*(519), 1111–1143. doi: 10.1002/qj.49712051902
Field, C. B., Jackson, R. B., & Mooney, H. A. (1995). Stomatal responses to increased CO2: Implications from the plant to the global scale. *Plant, Cell & Environment*, *18*(10), 1214–1225. doi: 10.1111/j.1365-3040.1995.tb00630.x
Fraedrich, K., Kleidon, A., & Lunkeit, F. (1999). A Green Planet versus a Desert World: Estimating the Effect of Vegetation Extremes on the Atmosphere. *Journal of Climate*, *12*(10), 3156–3163. doi: 10.1175/1520-0442(1999)012⟨3156:AGPVAD⟩2.0.CO;2
Garcia, E. S., Swann, A. L. S., Villegas, J. C., Breshears, D. D., Law, D. J., Saleska, S. R., & Stark, S. C. (2016). Synergistic ecoclimate teleconnections from forest loss in different regions structure global ecological responses. *PLoS ONE*, *11*(11), 1–12. doi: 10.1371/journal.pone.0165042
Geen, R., Lambert, F. H., & Vallis, G. K. (2018). Regime change behavior during Asian monsoon onset. *Journal of Climate*, *31*(8), 3327–3348. doi: 10.1175/JCLI-D-17-0118.1
Gregory, J. M. (2004). A new method for diagnosing radiative forcing and climate sensitivity. *Geophysical Research Letters*, *31*(3), L03205. doi: 10.1029/2003GL018747
Hansen, J., Sato, M., & Ruedy, R. (1997, March). Radiative forcing and climate response. *Journal of Geophysical Research: Atmospheres*, *102*(D6), 6831–6864. doi: 10.1029/96JD03436
Harris, C. R., Millman, K. J., van der Walt, S. J., Gommers, R., Virtanen, P., Cournapeau, D., … Oliphant, T. E. (2020, September). Array programming with NumPy. *Nature*, *585*(7825), 357–362. doi: 10.1038/s41586-020-2649-2
Held, I. M., & Soden, B. J. (2006, November). Robust Responses of the Hydrological Cycle to Global Warming. *Journal of Climate*, *19*(21), 5686–5699. doi: 10.1175/JCLI3990.1
Hobeichi, S., Abramowitz, G., & Evans, J. P. (2021). Robust historical evapotranspiration trends across climate regimes. *Hydrology and Earth System Sciences*, *25*(7), 3855–3874. doi: 10.5194/hess-25-3855-2021
Hoyer, S., & Hamman, J. (2017). Xarray: N-D labeled arrays and datasets in Python. *Journal of Open Research Software*, *5*(1). doi: 10.5334/jors.148
Hurley, J. V., & Boos, W. R. (2013, December). Interannual Variability of Monsoon Precipitation and Local Subcloud Equivalent Potential Temperature. *Journal of Climate*, *26*(23), 9507–9527. doi: 10.1175/JCLI-D-12-00229.1
Hurrell, J. W., Holland, M. M., Gent, P. R., Ghan, S., Kay, J. E., Kushner, P. J., … Marshall, S. (2013). The Community Earth System Model: A Framework for Collaborative Research. *Bulletin of the American Meteorological Society*, *94*(9), 1339–1360. doi: 10.1175/BAMS-D-12-00121.1
Jones, H. G. (1998). Stomatal control of photosynthesis and transpiration. *Journal of Experimental Botany*, *39*(SPECIAL ISSUE: STOMATAL BIOLOGY), 387–398.
Koster, R. D., Guo, Z., Dirmeyer, P. A., Bonan, G., Chan, E., Cox, P., … Yamada,

T. (2006). GLACE: The Global Land-Atmosphere Coupling Experiment. Part I: Overview. *Journal of Hydrometeorology*, *7*(4), 590–610. doi: 10.1175/JHM510.1

Kottek, M., Grieser, J., Beck, C., Rudolf, B., & Rubel, F. (2006). World map of the Köppen-Geiger climate classification updated. *Meteorologische Zeitschrift*, *15*(3), 259–263. doi: 10.1127/0941-2948/2006/0130

Laguë, M. M., Bonan, G. B., & Swann, A. L. S. (2019). Separating the Impact of Individual Land Surface Properties on the Terrestrial Surface Energy Budget in both the Coupled and Uncoupled Land–Atmosphere System. *Journal of Climate*, *32*(18), 5725–5744. doi: 10.1175/jcli-d-18-0812.1

Laguë, M. M., Pietschnig, M., Ragen, S., Smith, T. A., & Battisti, D. S. (2021). Terrestrial evaporation and global climate: Lessons from Northland, a planet with a hemispheric continent. *Journal of Climate*, *34*(6), 2253–2276. doi: 10.1175/jcli-d-20-0452.1

Laguë, M. M., & Swann, A. L. (2016). Progressive midlatitude afforestation: Impacts on clouds, global energy transport, and precipitation. *Journal of Climate*, *29*(15), 5561–5573. doi: 10.1175/jcli-d-15-0748.1

Laguë, M. M., Swann, A. L. S., & Boos, W. R. (2021). Radiative feedbacks on land surface change and associated tropical precipitation shifts. *Journal of Climate*(2012), 1–63. doi: 10.1175/jcli-d-20-0883.1

Lai, C.-T., & Katul, G. (2000, January). The dynamic role of root-water uptake in coupling potential to actual transpiration. *Advances in Water Resources*, *23*(4), 427–439. doi: 10.1016/S0309-1708(99)00023-8

Lawrence, D. M., Fisher, R. A., Koven, C. D., Oleson, K. W., Swenson, S. C., Bonan, G., … Zeng, X. (2019). The Community Land Model Version 5: Description of New Features, Benchmarking, and Impact of Forcing Uncertainty. *Journal of Advances in Modeling Earth Systems*, *11*(12), 4245–4287. doi: 10.1029/2018MS001583

Lemordant, L., Gentine, P., Swann, A. S., Cook, B. I., & Scheff, J. (2018). Critical impact of vegetation physiology on the continental hydrologic cycle in response to increasing CO2. *Proceedings of the National Academy of Sciences of the United States of America*, *115*(16), 4093–4098. doi: 10.1073/pnas.1720712115

Medlyn, B. E., Duursma, R. A., Eamus, DEREK., Ellsworth, D. S., Prentice, I. C., Barton, C. V. M., … Wingate, L. (2011). Reconciling the optimal and empirical approaches to modelling stomatal conductance. *Global Change Biology*, *17*(6), 2134–2144. doi: 10.1111/j.1365-2486.2010.02375.x

Monteith, J. (1965). Evaporation and environment. *Symposia of the Society for Experimental Biology*(19), 205–234.

Neale, R. B., Gettelman, A., Park, S., Chen, C.-C., Lauritzen, P. H., Williamson, D. L., … Others (2012). Description of the NCAR community atmosphere model (CAM 5.0). *NCAR Tech. Note NCAR/TN-486+STR.*

Neelin, J. D. (2007). Moist dynamics of tropical convection zones in monsoons, teleconnections, and global warming. In *The global circulation of the atmosphere* (pp. 267–301). doi: 10.2307/j.ctv1t1kg52

Neelin, J. D., & Held, I. M. (1987, January). Modeling tropical convergence based on the moist static energy budget. *Monthly Weather Review*, *115*(1), 3–12. doi: 10.1175/1520-0493(1987)115⟨0003:MTCBOT⟩2.0.CO;2

Nie, J., Boos, W. R., & Kuang, Z. (2010). Observational evaluation of a convective quasi-equilibrium view of monsoons. *Journal of Climate*, *23*(16), 4416–4428. doi: 10.1175/2010JCLI3505.1

Norby, R. J., Warren, J. M., Iversen, C. M., Medlyn, B. E., & McMurtrie, R. E. (2010). CO2 enhancement of forest productivity constrained by limited nitrogen availability. *Proceedings of the National Academy of Sciences of the United States of America*, *107*(45), 19368–19373. doi: 10.1073/pnas.1006463107

O'Gorman, P. A., & Muller, C. J. (2010a). How closely do changes in surface and column water vapor follow Clausius-Clapeyron scaling in climate change simulations? *Environmental Research Letters*, *5*(2). doi: 10.1088/1748-9326/5/2/025207

O'Gorman, P. A., & Muller, C. J. (2010b, April). How closely do changes in surface and column water vapor follow Clausius–Clapeyron scaling in climate change simulations? *Environmental Research Letters*, *5*(2), 025207. doi: 10.1088/1748-9326/5/2/025207

Pendergrass, A. G., Conley, A., & Vitt, F. M. (2018). Surface and top-of-Atmosphere radiative feedback kernels for cesm-cam5. *Earth System Science Data*, *10*(1), 317–324. doi: 10.5194/essd-10-317-2018

Pielke, R. A., Sr, ., Avissar, RonI., Raupach, M., Dolman, A. J., Zeng, X., & Denning, A. S. (1998, June). Interactions between the atmosphere and terrestrial ecosystems: Influence on weather and climate. *Global Change Biology*, *4*(5), 461–475. doi: 10.1046/j.1365-2486.1998.t01-1-00176.x

Privé, N. C., & Plumb, R. A. (2007). Monsoon dynamics with interactive forcing. Part II: Impact of eddies and asymmetric geometries. *Journal of the Atmospheric Sciences*, *64*(5), 1431–1442. doi: 10.1175/JAS3917.1

Raymond, D., Fuchs, Ž., Gjorgjievska, S., & Sessions, S. (2015, September). Balanced dynamics and convection in the tropical troposphere. *Journal of Advances in Modeling Earth Systems*, *7*(3), 1093–1116. doi: 10.1002/2015MS000467

Sellers, P. J., Bounoua, L., Collatz, G. J., a. Randall, D., a. Dazlich, D., Los, S. O., ... Others (1996). Comparison of radiative and physiological effects of doubled atmospheric CO2 on climate. *SCIENCE-NEW YORK THEN WASHINGTON-*, *271*(5254), 1402–1405. doi: 10.1126/science.271.5254.1402

Seneviratne, S. I., Corti, T., Davin, E. L., Hirschi, M., Jaeger, E. B., Lehner, I., ... Teuling, A. J. (2010, May). Investigating soil moisture–climate interactions in a changing climate: A review. *Earth-Science Reviews*, *99*(3-4), 125–161. doi: 10.1016/j.earscirev.2010.02.004

Shekhar, R., & Boos, W. R. (2016, July). Improving Energy-Based Estimates of Monsoon Location in the Presence of Proximal Deserts. *Journal of Climate*, *29*(13), 4741–4761. doi: 10.1175/JCLI-D-15-0747.1

Shell, K. M., Kiehl, J. T., & Shields, C. A. (2008). Using the radiative kernel technique to calculate climate feedbacks in NCAR's Community Atmospheric Model. *Journal of Climate*, *21*(10), 2269–2282. doi: 10.1175/2007JCLI2044.1

Sherwood, S. C., Roca, R., Weckwerth, T. M., & Andronova, N. G. (2010). Tropospheric water vapor, convection, and climate. *Reviews of Geophysics*, *48*(2), 1–29. doi: 10.1029/2009RG000301

Shukla, J., & Mintz, Y. (1982). Influence of Land-Surface Evapotranspiration on the Earth's Climate. *Science*, *215*(4539), 1498–1501. doi: 10.1126/science.215.4539.1498

Sobel, A. H., Bellon, G., & Bacmeister, J. (2007, November). Multiple equilibria in a single-column model of the tropical atmosphere. *Geophysical Research Letters*, *34*(22), L22804. doi: 10.1029/2007GL031320

Sobel, A. H., Nilsson, J., & Polvani, L. M. (2001, December). The Weak Temperature Gradient Approximation and Balanced Tropical Moisture Waves*. *Journal of the Atmospheric Sciences*, *58*(23), 3650–3665. doi: 10.1175/1520-0469(2001)058⟨3650:TWTGAA⟩2.0.CO;2

Sun, X., & Wang, G. (2022). Causes for the negative scaling of extreme precipitation at high temperatures. *Journal of Climate*, *35*(18), 6119–6134.

Swann, A. L. S., Fung, I. Y., & Chiang, J. C. H. (2012, January). Mid-latitude afforestation shifts general circulation and tropical precipitation. *Proceedings of the National Academy of Sciences*, *109*(3), 712–716. doi: 10.1073/pnas.1116706108

Swann, A. L. S., Fung, I. Y., Levis, S., Bonan, G. B., & Doney, S. C. (2010). Changes in Arctic vegetation amplify high-latitude warming through the greenhouse effect. *Proceedings of the National Academy of Sciences*, *107*(4), 1295–1300. doi: 10.1073/pnas.0913846107

Swann, A. L. S., Hoffman, F. M., Koven, C. D., & Randerson, J. T. (2016). Plant responses to increasing CO2 reduce estimates of climate impacts on drought severity. *PNAS*, *113*(36), 10019–10024. doi: 10.1073/pnas.1604581113

Swann, A. L. S., Laguë, M. M., Garcia, E. S., Breshears, D. D., Field, J., Moore, D., ... Minor, D. M. (2018). Local tree die-off impacts vegetation productivity across the US regardless of location via continental-scale ecoclimate teleconnections. *Environmental Research Letters*, *Submitted*.

Thomson, S. I., & Vallis, G. K. (2019). Hierarchical modeling of solar system planets with Isca. *Atmosphere*, *10*(12), 1–21. doi: 10.3390/ATMOS10120803

Trenberth, K. E. (1998). Atmospheric Moisture Residence Times and Cycling: Implications for Rainfall Rates and Climate Change. , *Climatic Change*(39), 667–694.

Vallis, G. K., Colyer, G., Geen, R., Gerber, E., Jucker, M., Maher, P., ... Thomson, S. I. (2018, March). Isca, v1.0: A framework for the global modelling of the atmospheres of Earth and other planets at varying levels of complexity. *Geoscientific Model Development*, *11*(3), 843–859. doi: 10.5194/gmd-11-843-2018

Vargas Zeppetello, L. R., Battisti, D. S., & Baker, M. B. (2019, October). The origin of soil moisture evaporation "regimes". *Journal of Climate*, *32*(20), 6939–6960. doi: 10.1175/JCLI-D-19-0209.1

Vial, J., Dufresne, J. L., & Bony, S. (2013). On the interpretation of inter-model spread in CMIP5 climate sensitivity estimates. *Climate Dynamics*, *41*(11-12), 3339–3362. doi: 10.1007/s00382-013-1725-9

Wang, Q., Cheng, L., Zhang, L., Liu, P., Qin, S., Liu, L., & Jing, Z. (2021). Quantifying the impacts of land-cover changes on global evapotranspiration based on the continuous remote sensing observations during 1982–2016. *Journal of Hydrology*, *598*(February), 126231. doi: 10.1016/j.jhydrol.2021.126231

Wilks, D. S. (2016, March). "The stippling shows statistically significant gridpoints": How Research Results are Routinely Overstated and Over-interpreted, and What to Do About It. *Bulletin of the American Meteorological Society*, 160309141232001. doi: 10.1175/BAMS-D-15-00267.1

Zelinka, M. D., Randall, D. A., Webb, M. J., & Klein, S. A. (2017). Clearing clouds of uncertainty. *Nature Climate Change*, *7*(10), 674–678. doi: 10.1038/nclimate3402

Supporting Information for: Reduced terrestrial evaporation increases atmospheric water vapor by generating cloud feedbacks

M. M. Laguë[1,2], G. R. Quetin[3], W. R. Boos[4,5]

[1]Coldwater Lab, Center for Hydrology, University of Saskatchewan, Canmore, AB, Canada
[2]Department of Atmospheric Sciences, University of Utah, Salt Lake City, UT, USA
[3]Department of Geography, University of California, Santa Barbara, CA, USA
[4]Department of Earth and Planetary Science, University of California, Berkeley, CA, USA
[5]Climate and Ecosystem Sciences Division, Lawrence Berkeley National Laboratory, Berkeley, CA, USA

Supplemental Figures

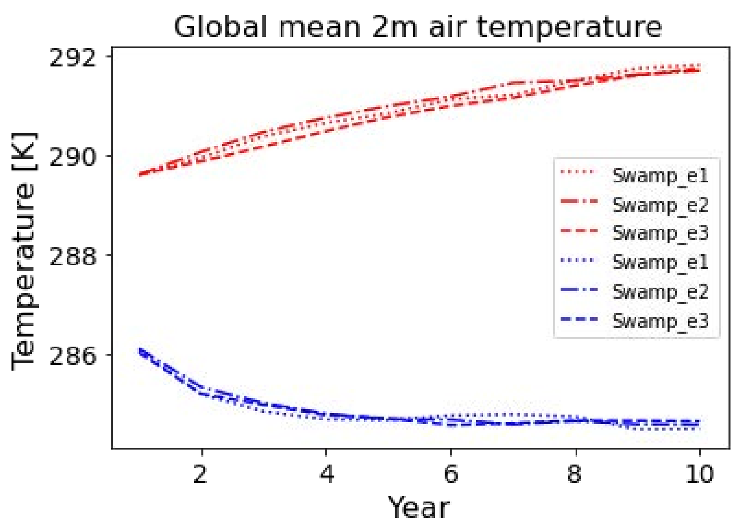

Figure S1. Spin-up of global mean 2m air temperatures across 3 ensemble members each of the Swamp and Desert simulations (swamp_e1-swamp_e3 and desert_e1-desert_e3, respectively), showing that the spread between ensemble members is small compared to inter-annual variability, and the difference between Swamp or Desert is much larger than the difference between ensemble members within either the Swamp or Desert simulation-type.

Corresponding author: M. M. Laguë, marysa.lague@usask.ca

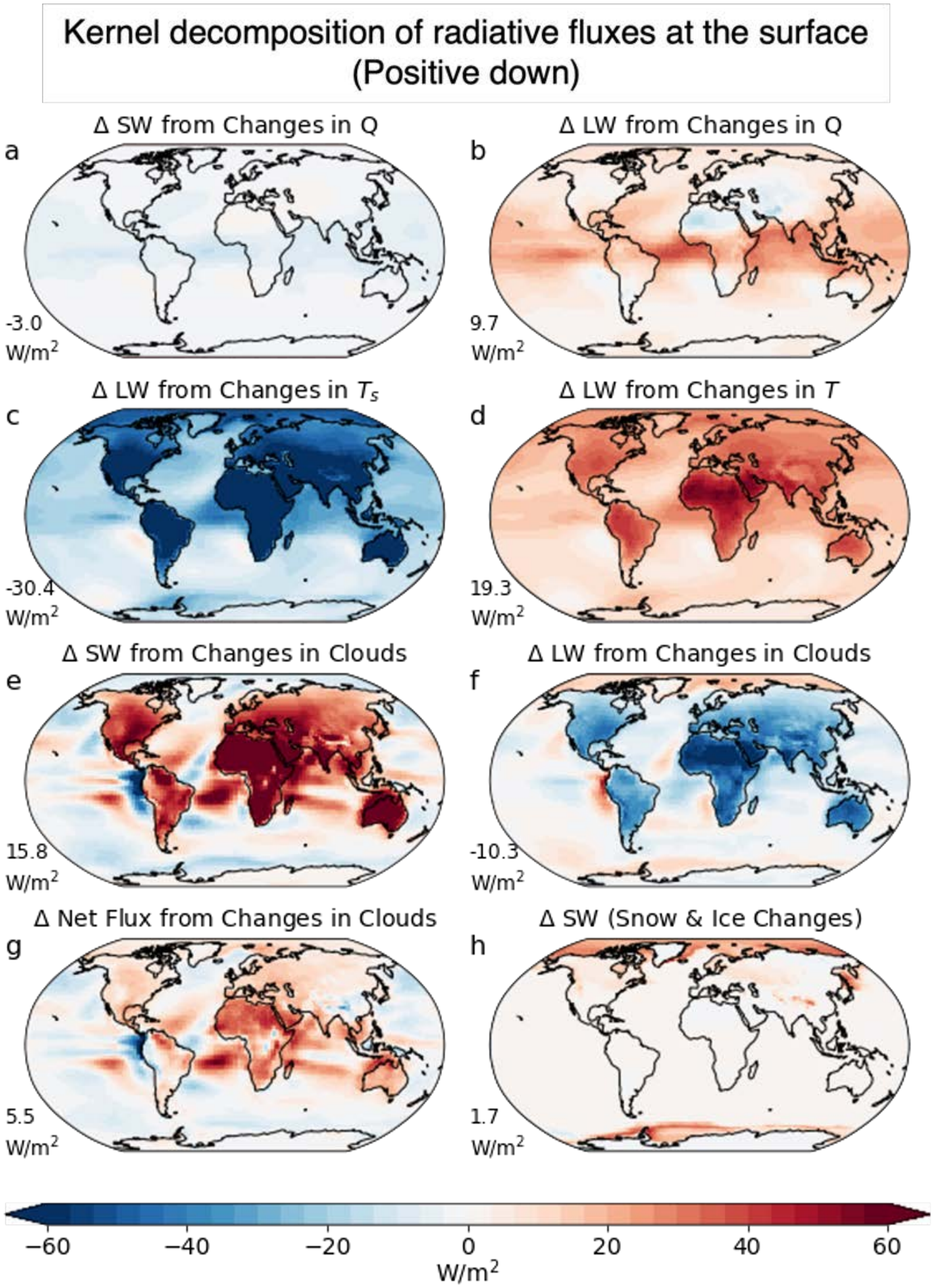

Figure S2. Decomposition of surface radiative fluxes using the radiative kernel for the DesertLand - SwampLand simulations. Fluxes are positive down into the surface, such that red regions indicate more energy into the surface attributable to that term in the DesertLand simulation than in the SwampLand simulation. The global mean value is noted to the lower left of each panel.

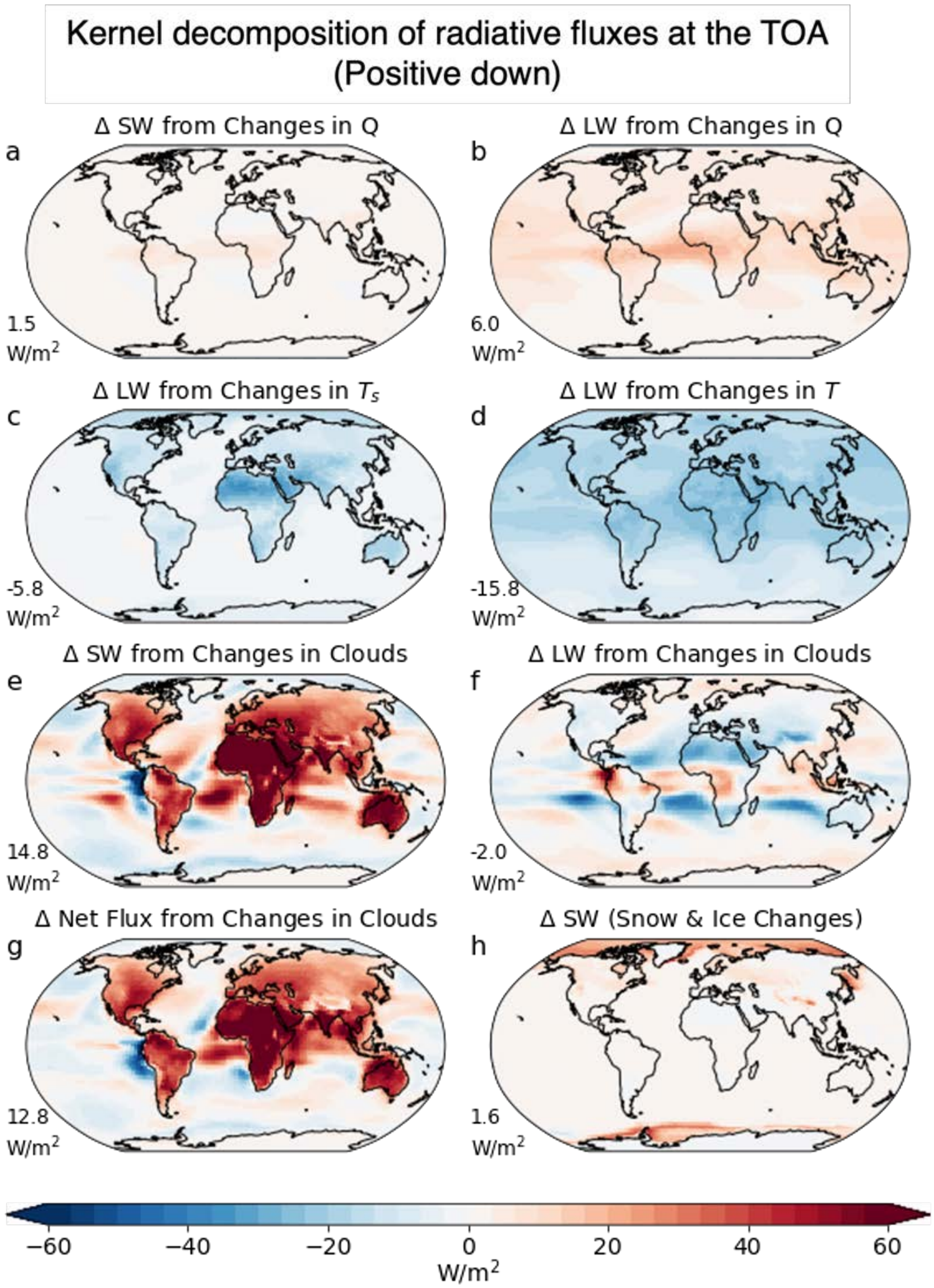

Figure S3. Decomposition of top of atmosphere radiative fluxes using the radiative kernel for the DesertLand - SwampLand simulations. Fluxes are positive down into the top of the atmosphere, such that red regions indicate more energy into the atmospheric column attributable to that term in the DesertLand simulation than in the SwampLand simulation. The global mean value is noted to the lower left of each panel.

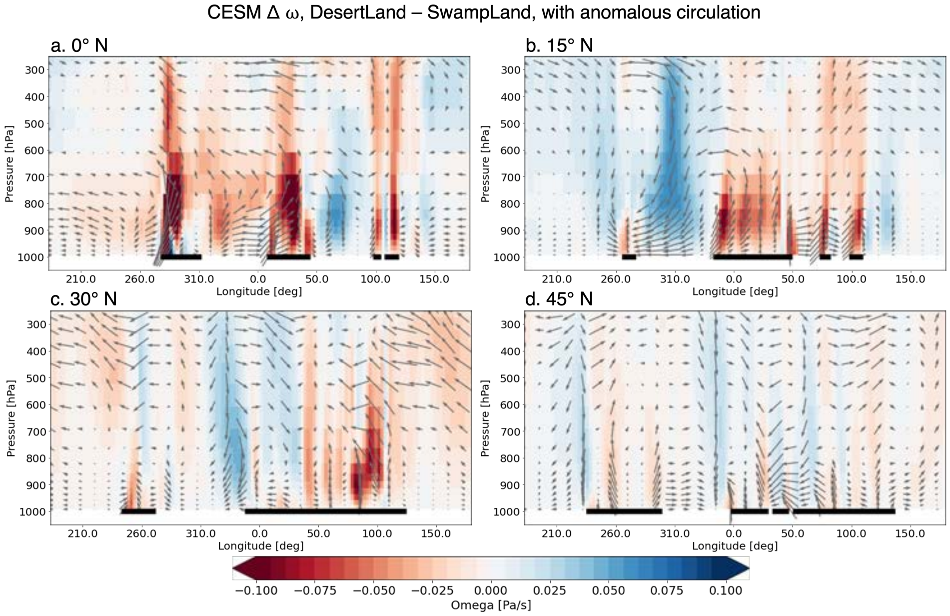

Figure S4. CESM vertical cross section (longitude vs. pressure) at various latitudes for the change in vertical motion ω [Pa/s] for DesertLand − SwampLand is shown in colors, with red indicating negative ω, i.e. positive vertical motion. Vectors show the direction of anomalous motion: u winds in [m/s] in the x-direction, and $\omega \times -150$ in [Pa/s] in the y direction. ω is multiplied by -1 so arrows point in the direction of motion, and by 50 so the vertical component is of comparable magnitude to the horizontal component, for ease of visualization. Horizontal black lines at the surface indicate land masses.

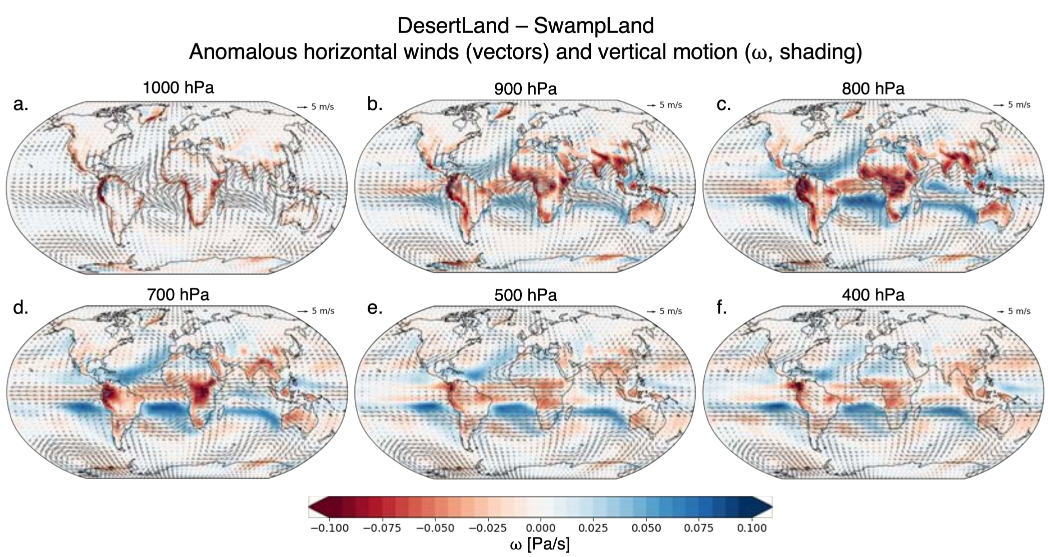

Figure S5. CESM change (DesertLand − SwampLand) in vertical motion ω [Pa/s] (shading, with red indicating upwards motion) and horizontal winds $\langle u, v \rangle$ [m/s] (vectors) at various levels of the atmosphere.

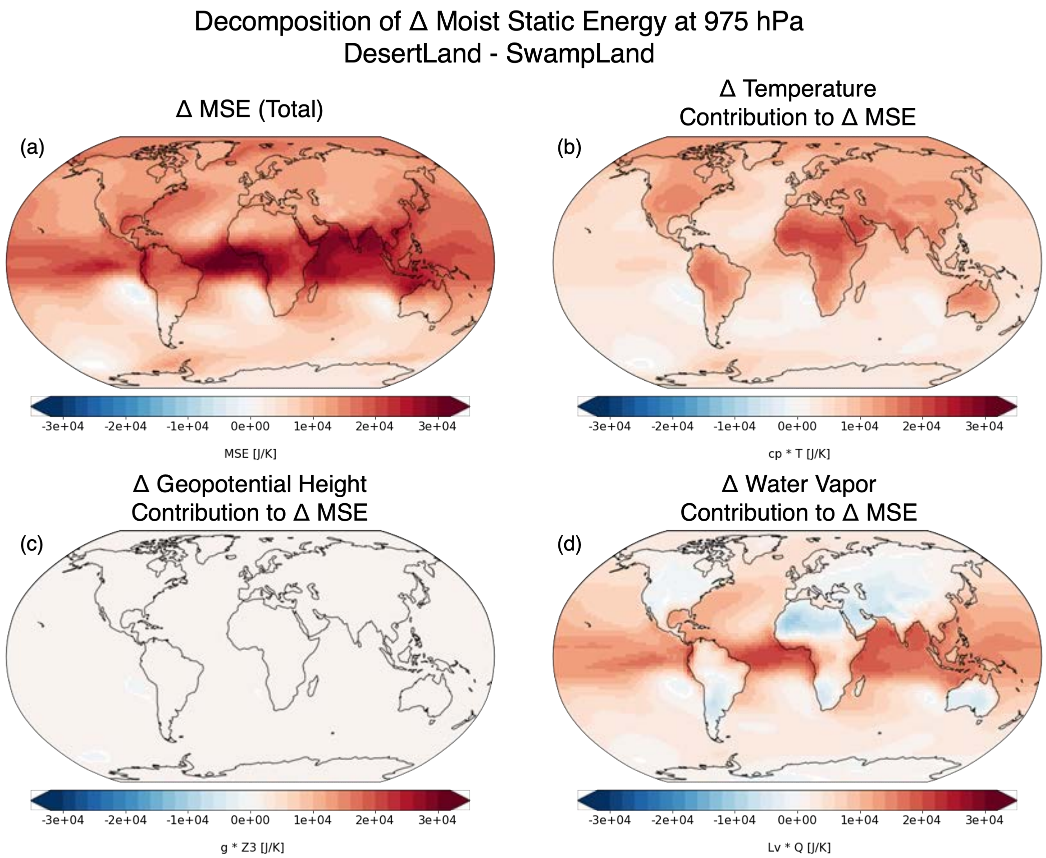

Figure S6. Decomposition of the change in moist static energy (MSE) into (a) the total and the components attributable to the change in (b) temperatures (c_pT), (c) geopotential heights (gZ), and (d) moisture (L_vQ)at 975 hPa, for the difference between the Desert and Swamp CESM simulations. Only changes that pass a statistical test are shown, where values are significant if the p-values calculated from a student's t-test pass a false discovery rate of 0.15.

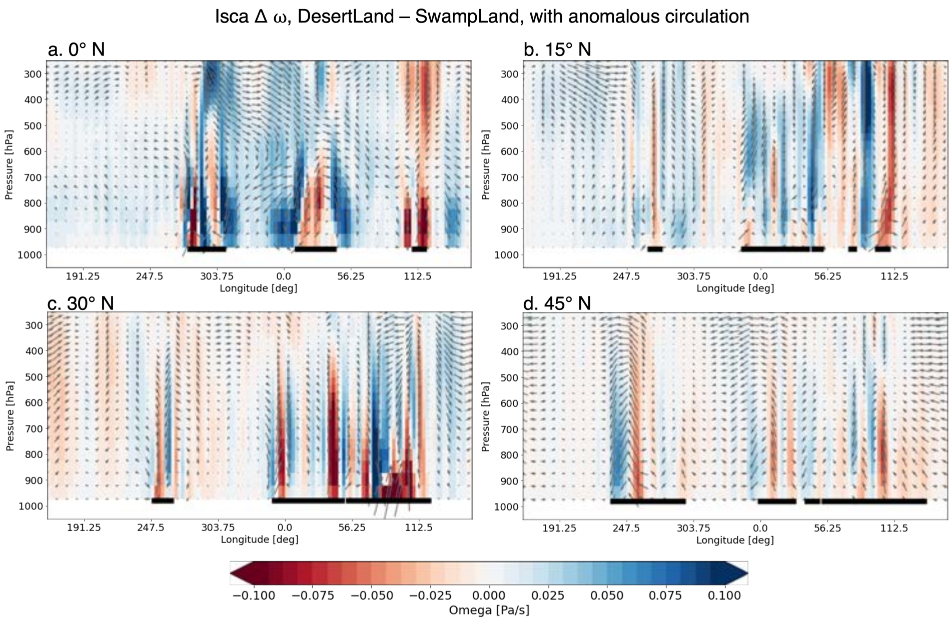

Figure S7. As in Fig. **??**, but for Isca.

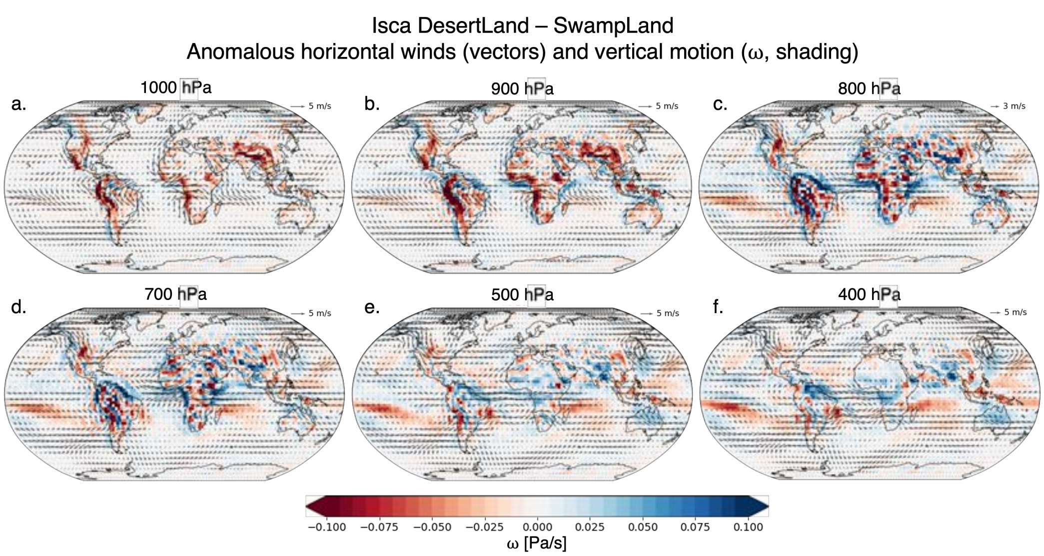

Figure S8. As in Fig. **??**, but for Isca.

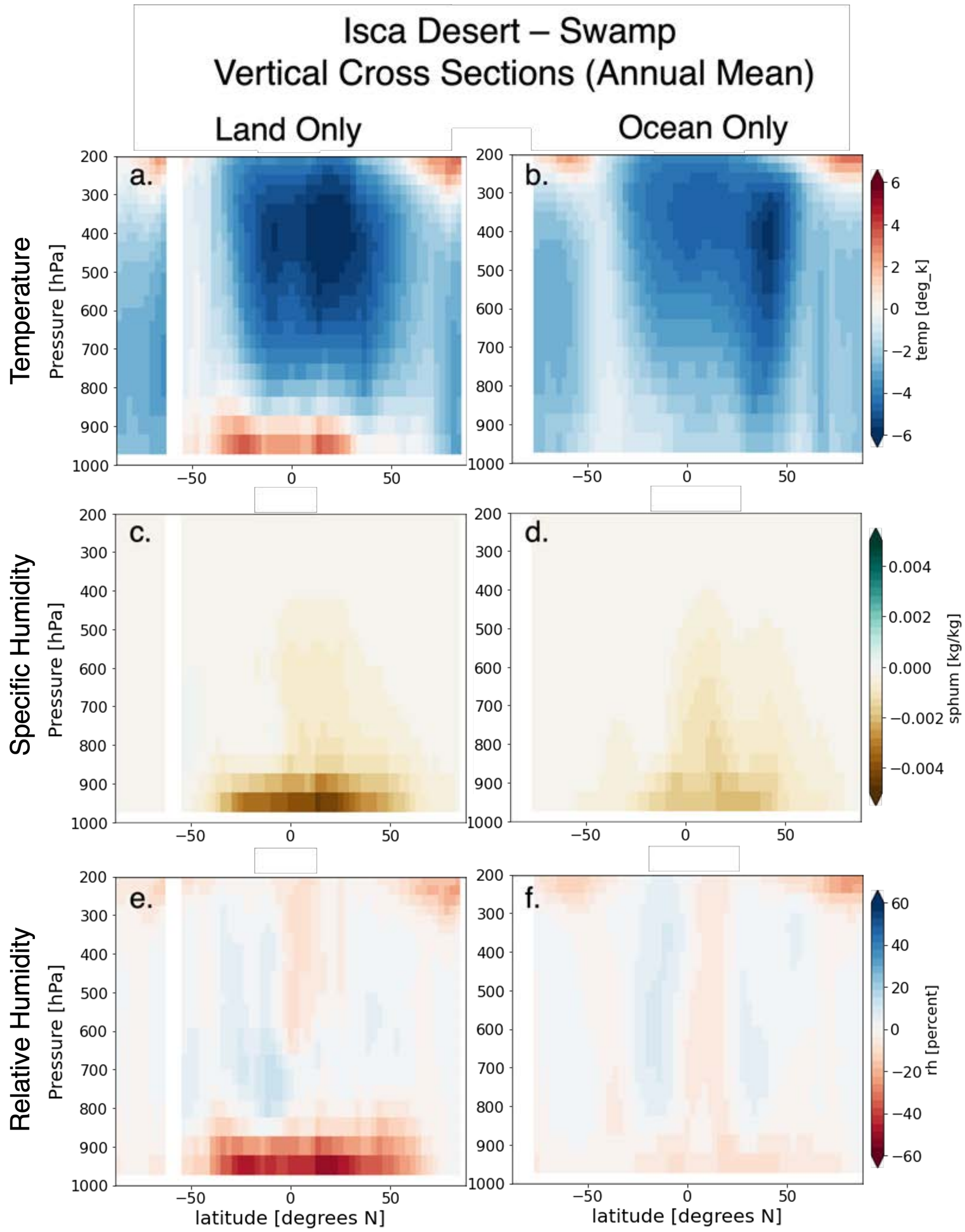

Figure S9. Change in the Isca simulations (DesertLand - SwampLand) in zonally averaged temperature (top), specific humidity (middle) and relative humidity (bottom) for land-only (left) and ocean-only (right).